Spatial exciton localization at interfaces of metal nanoparticles and atomically thin semiconductors

Robert Salzwedel,[1,*] Lara Greten,[1] Stefan Schmidt,[1] Stephen Hughes,[2] Andreas Knorr,[1] and Malte Selig[1]
[1]*Institut für Theoretische Physik, Nichtlineare Optik und Quantenelektronik, Technische Universität Berlin, 10623 Berlin, Germany*
[2]*Department of Physics, Queen's University, Kingston, Ontario, K7L 3N6, Canada*

(Received 18 May 2023; revised 6 December 2023; accepted 11 December 2023; published 30 January 2024)

We present a self-consistent Maxwell-Bloch theory to analytically study the interaction between a nanostructure consisting of a metal nanoparticle and a monolayer of transition-metal dichalcogenide. For the combined system, we identify an effective eigenvalue equation that governs the center-of-mass motion of the dressed excitons in a plasmon-induced potential. Examination of the dynamical equation of the exciton-plasmon hybrid reveals the existence of bound states with negative eigenenergies, which we interpret as excitons localized in the plasmon-induced potential. The appearance of these bound states in the potential indicates strong coupling between excitons and plasmons. We quantify this coupling regime by computing the scattered light in the near-field explicitly and identify signatures of strong exciton-plasmon coupling with an avoided crossing behavior and an effective Rabi splitting of tens of meV.

DOI: 10.1103/PhysRevB.109.035309

I. INTRODUCTION

Transition-metal dichalcogenides (TMDCs) exhibit remarkable optical properties, such as a direct band gap in the monolayer limit [1,2], valley-selective dichroism [3,4], and a spin-split band structure [4,5]. These properties, along with their high sensitivity to the surrounding environment [6–10], make them ideal for functionalization [11] with external nanoparticles, such as molecules [9,12–14], metal nanoparticles [15–17], quantum dots [18], or other two-dimensional (2D) materials [19–21], to locally tailor their optical properties.

Recently, many research works have focused on localizing excitons in TMDC layers through the deterministic creation of defects within the structure [22], strain-induced localization that attracts carriers [23,24], and Moiré potentials [25,26]. These methods enable the localization of individual excitons in TMDCs, making them promising candidates for single-photon emitters in 2D hybrid materials [22,27]. Moreover, the strong coupling of electromagnetic modes to quantum emitters provides unprecedented control over the quantum states, which may have applications, in particular when it reaches the quantum optics limit where light-matter effects cannot be explained semiclassically and multiphoton correlations are essential [28–30].

There has been much recent interest in creating joint states of excitonic and plasmonic excitations, known as *plexcitonic* states [31–34]; these hybrid states can be observed in strongly interacting systems that support both excitons and plasmons. Most works have focused on systems where an excitonic system is located inside a cavity to take advantage of the local field enhancement [35–38]. For example, picocavities have been utilized to achieve strong exciton-plasmon interaction [37–39]. Similarly, other systems have also reached the strong-coupling regime [40], evinced by a clear spectral splitting. However, the past few years have witnessed a significant surge in interest towards a variety of systems, in particular, systems consisting of individual nanoparticles interacting with excitonic systems, which were shown to reach the strong-coupling regime without requiring a typical dipole-cavity interaction commonly used in cavity QED [31–34]: In particular, experiments that are qualitatively similar to our theoretical study revealed impressive Rabi splittings on the

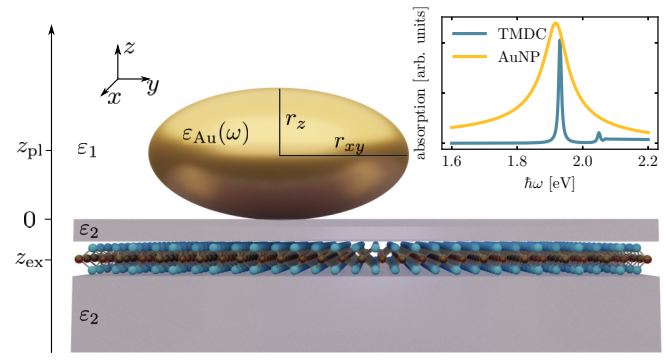

FIG. 1. *Coupled nanostructure.* The investigated system is composed of a gold nanoparticle with its center being located at z_{pl} and a two-dimensional TMDC monolayer at z_{ex}. The half spaces reveal a constant background permittivity ε_1 and ε_2, respectively, so that an interface exist at $z = 0$. The eccentricity of the AuNP can be manipulated from a sphere to an oblate spheroid which influences the interaction strength. The inset shows the absorption spectrum of the TMDC (blue) and the polarizability of a spheroidal gold nanoparticle. Using the permittivity function from Ref. [51] and Mie theory [52,53], the polarizability can be calculated classically.

*r.salzwedel@tu-berlin.de

order of 100 meV [41–43] for systems consisting of nanorods [44], resonators [37,45], nanodisks [42,46], bipyramids [43], and nanocubes [41].

On the theoretical side, these interacting systems are mostly treated using a classical coupled-mode theory with the interaction strength as fitting parameter [47,48]. However, there have been two recent studies that investigate the strong coupling of a metal nanorod with a TMDC monolayer [49,50] based on a quasinormal mode analysis and quantum reaction coordinate approach, respectively, which reproduce the experimentally observed spectral splittings [40,42,43]. However, the modifications of the excitonic properties are so far not well investigated.

In this paper, we consider a hybrid nanostructure consisting of a spheroidal gold nanoparticle (AuNP) and a monolayer of transition-metal dichalcogenides (TMDC), as illustrated in Fig. 1. To model this system in a quantitative way, both the TMDC and the AuNP are encapsulated in two different media with homogeneous and isotropic permittivities ε_1 and ε_2, respectively. In contrast with previous works, we treat the entire system using a semiclassical microscopic model based on the Maxwell-Heisenberg equation of motion framework. We analytically identify an eigenvalue equation in the composite system, which describes the center-of-mass motion of the excitons in the potential induced by the plasmonic excitation. Our derived eigenvalue equation can be used to drastically reduce the numerical complexity of the problem, and offers new physical insight into the character of the hybridization. As an example, it allows us to connect to the strong-coupling limit with the occurrence of bound exciton states induced by the AuNP.

The rest of our paper is organized as follows: In Sec. II, we give an introduction to the theoretical description of the composite subsystems: We provide the excitonic Bloch equation for TMDC excitons in Sec. II A and discuss Mie-Gans theory for the localized plasmons in the AuNP in Sec. II B. We proceed with introducing a Green's function solution of Maxwell's equations in Sec. II C that is used to couple the constituents and find equations that describe the dynamics of the coupled system. In Sec. III, we discuss the occurring eigenvalue equation that characterizes the interaction within the nanoparticle and analyze the corresponding eigenvalues and eigenvectors. In Sec. IV, we then study the implications of the interaction and the arising eigenstates on the macroscopic polarization within the TMDC monolayer. Section V computes the electric near-field around the nanostructures and finds a peak splitting of the excitonic and plasmonic modes that for artificially detuned exciton resonance is shown to result in an avoided crossing behavior of the two resonances. Finally, in Sec. VI, we provide our conclusions and discuss the utility of our analytical plexcitonic approach to describe the interaction in nanostructures and their implications on localization and strong coupling.

II. MAXWELL-BLOCH APPROACH

We employ a semiclassical framework to obtain a set of self-consistent Maxwell-Bloch equations. These describe the exciton dynamics in terms of excitonic Bloch equations, the plasmonic response of the metal nanoparticle using Mie theory and the electromagnetic field that mediates the interaction by Maxwell's equations. We work in real space for the out-of-plane component (z direction) and Fourier transform the in-plane component (x, y directions) and transform the temporal dynamics to the frequency domain so that we use a set of $(\mathbf{Q}_\parallel, z; \omega)$ as our coordinates, which makes it possible to solve the differential equations algebraically.

A. Optical response of transition-metal dichalcogenide excitons

The microscopic dynamics in TMDC monolayers are described using the Heisenberg equation of motion, which leads to excitonic Bloch equations, as described in Refs. [54–56]:

$$\left(E^\nu + \frac{\hbar^2 \mathbf{Q}_\parallel^{\,2}}{2M} - \hbar\omega - i\gamma^\nu\right) p^{\xi\nu}_{\mathbf{Q}_\parallel}(\omega) = \varphi^*_\nu(\mathbf{r}_\parallel = \mathbf{0})\,(\mathbf{d}^\xi)^* \cdot \mathbf{E}_{\mathbf{Q}_\parallel}(z_{\mathrm{ex}};\,\omega). \tag{1}$$

The left-hand side accounts for the oscillation of the microscopic polarization $p^{\xi\nu}_{\mathbf{Q}_\parallel}$ with excitonic energy E^ν, where we use a valley index $\xi = +1$ (-1) for the K (K') valley, respectively, exciton state number ν, e.g., $1s$, $2s$, ..., and Fourier component of the center-of-mass motion $\mathbf{Q}_\parallel$. Furthermore, the left-hand side accounts for the dispersion of excitons (second term) with the exciton mass M. The dephasing rates γ^ν are added to account for phonon-induced dephasing as calculated microscopically in Ref. [57]. The TMDC excitons are driven by the electric field $\mathbf{E}_{\mathbf{Q}_\parallel}(z_{\mathrm{ex}};\,\omega)$ via the electronic transition dipole moment $\mathbf{d}^\xi$ at the respective valley [4] and $\varphi_\nu(\mathbf{r}_\parallel = \mathbf{0})$. Here, $\varphi_\nu(\mathbf{r}_\parallel)$ is the excitonic wave function depending on the relative coordinate of electron and hole $\mathbf{r}_\parallel$ and can be obtained by solution of the Wannier equation with a Coulomb potential tailored to the specific geometry. In the literature, this is mostly done using a Rytova-Keldysh-type approach [6,7] with a model dielectric function [58,59], which we adapt to our effective four-layer system, cf. Fig. 1. The excitonic wave function is evaluated at $\mathbf{r}_\parallel = \mathbf{0}$ which accounts for the probability of finding electron and hole at the same position [60]. The resulting TMDC absorption spectrum is given in the inset of Fig. 1. In the hybrid structure, the total field at the TMDC position $\mathbf{E}_{\mathbf{Q}_\parallel}(z_{\mathrm{ex}})$ includes the external field $\mathbf{E}^0_{\mathbf{Q}_\parallel}$, a contribution caused by the AuNP-TMDC interaction as well as the valley exchange coupling within the monolayer [61].

The microscopic TMDC polarization $p^{\xi\nu}_{\mathbf{Q}_\parallel}$, calculated from Eq. (1), is related to the macroscopic polarization via

$$\mathbf{P}^{\mathrm{TMDC}}_{\mathbf{Q}_\parallel}(z;\,\omega) = \sum_{\xi\nu} \mathbf{d}^\xi\, \varphi_\nu(\mathbf{r}_\parallel = \mathbf{0})\, p^{\xi\nu}_{\mathbf{Q}_\parallel}(\omega)\, \delta(z - z_{\mathrm{ex}}) + \mathrm{c.c.}, \tag{2}$$

where we assume that the monolayer can be approximated as infinitesimally thin which makes it effectively two dimensional. This definition will be used as a source term in the macroscopic Maxwell's equation. Later in this paper, we only focus on the $\nu = 1s$ resonance and effectively drop the ν index. This is a good approximation when the $1s$ resonance is spectrally clearly separated and the spectral range is limited to the one dominated by the $1s$ resonance, as it is for our case.

TABLE I. Material parameters for $MoSe_2$ and AuNP used in the numerical implementation.

Parameter	Value	Units	Reference
d	0.27	eC nm	[4]
M	6.2535	fs^2 eV nm^{-2}	[85]
$\hbar\gamma$ (300 K)	0.0269	eV	[a]
c	299.79246	nm fs^{-1}	
φ_0	0.51	nm^{-1}	[b]
ϵ_∞	1.53		[51]
$\hbar\omega_p$	8.55063	eV	[51]
$\hbar\gamma_p$	0.072932	eV	[51]
A_1	0.94		[51]
φ_1	$-\pi/4$		[51]
$\hbar\omega_1$	2.64923	eV	[51]
$\hbar\gamma_1$	0.53906	eV	[51]
A_2	1.36		[51]
φ_2	$-\pi/4$		[51]
$\hbar\omega_2$	3.74575	eV	[51]
$\hbar\gamma_2$	1.31898	eV	[51]
r_{xy}	8	nm	
r_z	4	nm	
z_{ex}	−1	nm	
z_{pl}	5	nm	
ε_1	4.5		
ε_2	1		

[a]Calculated by exploiting the method from Ref. [57].
[b]Calculated from Rytova approach for 4 layer system similar to Ref. [6].

B. Optical response of nanoparticle plasmons

The metal nanoparticle, in the dipole approximation, is modeled using Mie-Gans theory [52,53] that condenses the light-matter interaction in response to the external field $\mathbf{E}^0_{\mathbf{Q}_\parallel}$ for a spheroid in a diagonal polarizability tensor $\boldsymbol{\alpha}(\omega)$ whose diagonal components are given by

$$\alpha_i(\omega) = 4\pi\varepsilon_0\varepsilon_1 \frac{r_x r_y r_z}{3} \frac{\varepsilon_{\mathrm{Au}}(\omega) - \varepsilon_1}{L_i\varepsilon_{\mathrm{Au}}(\omega) + \varepsilon_1(1 - L_i)}. \tag{3}$$

The gold permittivity $\varepsilon_{\mathrm{Au}}(\omega)$ is analytically modeled using the approach from Ref. [51], that incorporates d band contributions and two interband transitions in the visible regime in order to accurately describe the experimental data found in Ref. [62]. Its analytical expression is given in Eq. (A1). The strength of the individual components depends on the aspect ratio and is determined by the lengths of the spheroid's semi-axes r_i and L_i, as defined in Eqs. (A2) and (A3). This description is valid for the nanoparticles considered in our study; for smaller or larger nanoparticles one would need to include additional terms to incorporate hydrodynamic [63,64] or retardation effects [65–67].

The choice of an oblate spheroid allows for enhanced interaction of AuNP and TMDC since it reduces the effective separation while keeping the volume and thus the polarizability large. In the inset of Fig. 1, the absolute value of the in-plane polarizability of the considered spheroid is shown as an example. All used parameters can be found in Table I. The dipole approximation is generally applicable for metal nanoparticles significantly smaller than the wavelength of the incident light. This condition ensures that the electromagnetic field across the nanoparticle remains approximately uniform, allowing for an effective representation of the particle as a single dipole. In our study, the dimensions of the particles under consideration have a radius of $r_{xy} = 8$ nm. These length scales are at least an order of magnitude smaller than the relevant wavelength range from 500 to 700 nm. Furthermore, one might assume that higher-order modes occurring in the metal nanoparticle become important due to the small interparticle spacing of TMDC and AuNP of 1 nm for our study. However, due to the far-field excitation and the fact that the unstructured excitons within the 2D semiconductor corresponds to a collective continuum of emitters large compared with single atoms, as discussed in Ref. [68], the dipole mode is the dominant contribution. Therefore, for a qualitative and even a quantitative understanding [16,31,68–73] of the interaction between a plasmonic nanoparticle (dipole source) and the calculated localization of excitons (TMDC monolayer), which is of primary interest in this study, it is sufficient to assume the dipole approximation. For other scenarios, such as excitation by point dipoles, it might be necessary to go beyond the dipole approximation [65].

In this dipole approximation, the AuNP polarization can be written as

$$\mathbf{P}^{\mathrm{AuNP}}_{\mathbf{Q}_\parallel}(z;\,\omega) = \frac{\boldsymbol{\alpha}(\omega)}{(2\pi)^2} \cdot \int \mathrm{d}^2\mathbf{Q}'_\parallel\, e^{-i(\mathbf{Q}_\parallel - \mathbf{Q}'_\parallel)\cdot\mathbf{r}^{\mathrm{pl}}_\parallel}\, \mathbf{E}_{\mathbf{Q}'_\parallel}(z_{\mathrm{pl}};\omega)\delta(z - z_{\mathrm{pl}}), \tag{4}$$

which describes the polarization of a point dipole located at $\mathbf{r}_{\mathrm{pl}} = (\mathbf{r}^{\mathrm{pl}}_\parallel, z_{\mathrm{pl}})$. The polarizability $\boldsymbol{\alpha}(\omega)$ incorporates the electric field generated by the AuNP. Thus, $\mathbf{E}_{\mathbf{Q}'_\parallel}(z_{\mathrm{pl}})$ corresponds to the electric field at the position of the AuNP, excluding the field contributed by itself. For the purpose of this paper, we assume $\mathbf{r}^{\mathrm{pl}}_\parallel = 0$. Combing the two polarizations given in Eqs. (2) and (4), the full polarization is given by

$$\mathbf{P}_{\mathbf{Q}_\parallel}(z;\,\omega) = \mathbf{P}^{\mathrm{TMDC}}_{\mathbf{Q}_\parallel}(z;\,\omega) + \mathbf{P}^{\mathrm{AuNP}}_{\mathbf{Q}_\parallel}(z;\,\omega), \tag{5}$$

which enters Maxwell's equations to compute the electric field close to the nanostructure.

C. Optical response of the coupled nanostructures

In our description, the interaction of TMDC and AuNP is mediated by the electric field, as can be seen in Eqs. (1) and (4), which has to be determined self-consistently from Maxwell's equations. The starting point for the investigation is the wave equation

$$\left(\nabla^2 - \frac{\varepsilon(z)}{c^2}\frac{\partial^2}{\partial t^2}\right)\mathbf{E}(\mathbf{r},t) = \frac{1}{\varepsilon_0 c^2}\frac{\partial^2}{\partial t^2}\mathbf{P}(\mathbf{r},t) - \frac{1}{\varepsilon(z)\varepsilon_0}\nabla[\nabla\cdot\mathbf{P}(\mathbf{r},t)], \tag{6}$$

for polarization $\mathbf{P}(\mathbf{r},t)$ in a background medium with spatially piecewise constant permittivity $\varepsilon(z)$, which is ε_1 in the upper half plane and ε_2 in the lower half plane.

A general solution of this equation can be provided via the Green's function using the coordinate system $(\mathbf{Q}_\parallel, z; \omega)$ which we obtain by Fourier transformation $\mathbf{E}(\mathbf{r}; \omega) = (2\pi)^{-2} \int \mathrm{d}^2\mathbf{Q}_\parallel e^{i\mathbf{Q}_\parallel \cdot \mathbf{r}_\parallel} \mathbf{E}_{\mathbf{Q}_\parallel}(z; \omega)$, with

$$\mathbf{E}_{\mathbf{Q}_\parallel}(z; \omega) = \int_{\mathbb{R}} \mathrm{d}z' \mathcal{G}_{\mathbf{Q}_\parallel}(z, z'; \omega) \cdot \mathbf{P}_{\mathbf{Q}_\parallel}(z'; \omega) + \mathbf{E}^0_{\mathbf{Q}_\parallel}(z; \omega), \tag{7}$$

with the dyadic Green's function $\mathcal{G}_{\mathbf{Q}_\parallel}(z, z'; \omega)$ and the external electric field $\mathbf{E}^0_{\mathbf{Q}_\parallel}(z; \omega)$. For Eq. (6), the dyadic Green's function is given by

$$\mathcal{G}_{\mathbf{Q}_\parallel}(z, z'; \omega) = \left[-\frac{\omega^2}{\varepsilon_0 c^2} \mathbb{1} + \frac{1}{\varepsilon_0 \varepsilon(z)} \begin{pmatrix} \mathbf{Q}_\parallel \otimes \mathbf{Q}_\parallel & i\mathbf{Q}_\parallel \partial_{z'} \\ i\mathbf{Q}_\parallel^T \partial_{z'} & \partial_{z'}^2 \end{pmatrix} \right] \times G_{\mathbf{Q}_\parallel}(z, z'; \omega), \tag{8}$$

where the symbol $\mathbb{1}$ denotes the three-dimensional identity matrix. The second matrix has a two-by-two matrix as its first entry, and the resulting matrix is also three dimensional. Here, the scalar Green's function $G_{\mathbf{Q}_\parallel}(z, z'; \omega)$ is defined as

$$G_{\mathbf{Q}_\parallel}(z, z'; \omega) = -\frac{i}{2k_{\mathbf{Q}_\parallel}} e^{ik_{\mathbf{Q}_\parallel}|z-z'|}, \tag{9}$$

where $k_{\mathbf{Q}_\parallel} \equiv [\varepsilon(z)\frac{\omega^2}{c^2} - Q_\parallel^2]^{1/2}$. Equations (8) and (9) allow one to calculate the self-consistent electric field at the TMDC and the AuNP position which enters the dynamical equation for the microscopic TMDC polarization $p^{\xi\nu}_{\mathbf{Q}_\parallel}(\omega)$, cf. Eq. (1), and the AuNP polarization, cf. Eq. (4).

We focus on the $1s$ TMDC resonance in our interacting system and, for clarity, we omit the index ν. We use the notation $\varphi^{1s}(\mathbf{r}_\parallel = 0) \to \varphi_0$ to represent the value of φ^{1s} at the origin and the corresponding $1s$ damping coefficient γ. By inserting Eq. (7) into Eq. (1), we find the following equation of motion for the microscopic TMDC polarization:

$$\begin{aligned} \left[E^{1s} + \frac{\hbar^2 \mathbf{Q}_\parallel^2}{2M} - \hbar\omega - i\gamma \right] p^{\xi}_{\mathbf{Q}_\parallel}(\omega) &= \varphi_0^* \, \mathbf{d}^{\xi *} \cdot \left[\mathbf{E}^0_{\mathbf{Q}_\parallel}(z_{\mathrm{ex}}; \omega) + \mathcal{G}_{\mathbf{Q}_\parallel}(z_{\mathrm{ex}}, z_{\mathrm{pl}}; \omega) \cdot \boldsymbol{\alpha}(\omega) \cdot \mathbf{E}^0(\mathbf{r}_{\mathrm{pl}}; \omega) \right] \\ &+ |\varphi_0|^2 \mathbf{d}^{\xi *} \cdot \sum_{\xi'} \Big[\mathcal{G}_{\mathbf{Q}_\parallel}(z_{\mathrm{ex}}, z_{\mathrm{ex}}; \omega) \cdot \mathbf{d}^{\xi'} p^{\xi'}_{\mathbf{Q}_\parallel}(\omega) \\ &+ \mathcal{G}_{\mathbf{Q}_\parallel}(z_{\mathrm{ex}}, z_{\mathrm{pl}}; \omega) \cdot \frac{\boldsymbol{\alpha}(\omega)}{(2\pi)^2} \cdot \int \mathrm{d}^2\mathbf{Q}'_\parallel \, \mathcal{G}_{\mathbf{Q}'_\parallel}(z_{\mathrm{pl}}, z_{\mathrm{ex}}; \omega) \cdot \mathbf{d}^{\xi'} p^{\xi'}_{\mathbf{Q}'_\parallel}(\omega) \Big]. \end{aligned} \tag{10}$$

In Eq. (10), the coupling between TMDC excitons and the AuNP plasmon induced by the electric field is given in terms of the Green's functions, including the self-interaction of the excitonic polarization. In Eq. (10), the first term on the right-hand side is the interaction with the external electric field $\mathbf{E}^0_{\mathbf{Q}_\parallel}(z_{\mathrm{ex}})$ at the TMDC position z_{ex}. The second term is the external electric field at the AuNP position, which is resonantly enhanced by the AuNP and then coupled to the TMDC. In the second line, we see that the electric field also mediates a dipole-dipole coupling between the excitons at the K and K' points, widely known as the valley exchange coupling [74]. The final term in the equation describes a self-interaction of the TMDC that is mediated by the AuNP, as evinced by the appearance of two Green's functions. This term can be interpreted as an effective exciton-exciton interaction.

In our particular setup, special care is required to include the dielectric interface at $z = 0$, which arises due to the piecewise constant background permittivity. Since the distance between the TMDC and the AuNP is only a few nanometers and the wavelengths used are in the optical range, we have opted to utilize the quasistatic Green's function, provided in Eq. (C1), which also incorporates the change in background permittivity. This leads to the fact that the quasistatic Green's function can only be defined piecewise. Due to the interface, the Green's function also contains additional mirror charge terms. The Green's function is derived following Ref. [75] and takes into account the individual positions of the scatterers.

In the quasistatic limit, i.e., $c \to \infty$, the dyadic Green's function can be expressed as

$$\mathcal{G}^{\mathrm{st}}_{\mathbf{Q}_\parallel}(z, z') = \frac{1}{\varepsilon_0 \varepsilon(z)} \begin{pmatrix} \mathbf{Q}_\parallel \otimes \mathbf{Q}_\parallel & i\mathbf{Q}_\parallel \partial_{z'} \\ i\mathbf{Q}_\parallel^T \partial_{z'} & \partial_{z'}^2 \end{pmatrix} G^{\mathrm{st}}_{\mathbf{Q}_\parallel}(z, z'). \tag{11}$$

Evaluating Eq. (10) with the quasistatic scalar Green's function $G^{\mathrm{st}}_{\mathbf{Q}_\parallel}(z, z')$ in Eq. (C1), we obtain individual equations for the respective valley K and K'. To investigate the effects resulting from the coupling of TMDC and AuNP, we first diagonalize our system of equations by performing a transformation with respect to the exchange coupling [first term in the second line in Eq. (10)]:

$$\begin{pmatrix} p^U_{\mathbf{Q}_\parallel} \\ p^V_{\mathbf{Q}_\parallel} \end{pmatrix} \equiv \frac{1}{\sqrt{2}} \begin{pmatrix} -e^{i\phi} & e^{-i\phi} \\ e^{i\phi} & e^{-i\phi} \end{pmatrix} \cdot \begin{pmatrix} p^K_{\mathbf{Q}_\parallel} \\ p^{K'}_{\mathbf{Q}_\parallel} \end{pmatrix}, \tag{12}$$

similar to Ref. [61] with ϕ being the angle coordinate in polar coordinate corresponding to $\mathbf{Q}_\parallel$. The same matrix transformation is used to transform the circularly polarized external electric field $\mathbf{E}^0_{\mathbf{Q}_\parallel}$ in Eq. (10) into its new basis $\{E^{0,U}_{\mathbf{Q}_\parallel}, E^{0,V}_{\mathbf{Q}_\parallel}\}$. We find two decoupled equations, Eqs. (13) and (14), for the new polarizations $p^U_{\mathbf{Q}_\parallel}(\omega)$ and $p^V_{\mathbf{Q}_\parallel}(\omega)$:

$$\left[E^{1s} + \frac{\hbar^2 \mathbf{Q}_\parallel^2}{2M} - \hbar\omega - i\gamma \right] p^U_{\mathbf{Q}_\parallel}(\omega) = d^* \varphi_0^* \, E^{0,U}_{\mathbf{Q}_\parallel}(z_{\mathrm{ex}}; \omega). \tag{13}$$

In Eq. (13), $p^U_{\mathbf{Q}_\parallel}$ is unaffected by the exchange coupling. The left-hand side of Eq. (13) exhibits a free parabolic exciton

dispersion that is consistent with previous literature [61]. Accordingly, we refer to Eq. (13) as parabolic Bloch equation. It is worth noting that both the exchange coupling contributions and the coupling contributions between TMDC and AuNP cancel each other out. This is due to the quasistatic approach, which reduces the interaction to longitudinal components that appear under the transformation in Eq. (12) only in the V component, cf. Ref. [61]. Hence, the right-hand side only accounts for the excitation by the external electric field $E^{0,U}_{\mathbf{Q}_\parallel}(z_{\mathrm{ex}};\omega)$ at the TMDC position and accordingly has the same form as the pristine TMDC case without exchange and TMDC-AuNP coupling. In contrast, the equation for $p^V_{\mathbf{Q}_\parallel}(\omega)$, Eq. (14), reads

$$\begin{aligned}\Big[E^{1s}+\tfrac{\hbar^2\mathbf{Q}_\parallel^2}{2M}+X_{\mathbf{Q}_\parallel}(z_{\mathrm{ex}})-\hbar\omega-i\gamma\Big]p^V_{\mathbf{Q}_\parallel}(\omega)\\ -\tfrac{1}{(2\pi)^2}\int \mathrm{d}^2\mathbf{Q}'_\parallel\, V_{\mathbf{Q}_\parallel\mathbf{Q}'_\parallel}(z_{\mathrm{ex}},z_{\mathrm{pl}};\omega)\,p^V_{\mathbf{Q}'_\parallel}(\omega)\\ = d^*\varphi_0^*\left(E^{0,V}_{\mathbf{Q}_\parallel}(z_{\mathrm{ex}};\omega)+S_{\mathbf{Q}_\parallel}(z_{\mathrm{pl}},z_{\mathrm{ex}};\omega)\right).\end{aligned} \tag{14}$$

Comparing with Eq. (13), where all interaction contributions cancel, we find three additional terms. The first one is the valley exchange term, which renormalizes the parabolic dispersion:

$$X_{\mathbf{Q}_\parallel}(z_{\mathrm{ex}})=-|\varphi_0|^2|d|^2\frac{Q_\parallel^2}{\varepsilon_0\varepsilon_2}G^{\mathrm{st}}_{\mathbf{Q}_\parallel}(z_{\mathrm{ex}},z_{\mathrm{ex}}). \tag{15}$$

As can be seen in Fig. 2, where we depict the further relevant momentum range from $-1\ \mathrm{nm}^{-1}$ to $1\ \mathrm{nm}^{-1}$, $X_{\mathbf{Q}_\parallel}(z_{\mathrm{ex}})$ changes the parabolic dispersion to a conical one depending on the exchange coupling among the K and K' valleys, cf. Ref. [61]. Hence, we refer to Eq. (14) as the conical Bloch equation. The other additional terms $V_{\mathbf{Q}_\parallel\mathbf{Q}'_\parallel}(z_{\mathrm{ex}},z_{\mathrm{pl}};\omega)$ and $S_{\mathbf{Q}_\parallel}(z_{\mathrm{pl}},z_{\mathrm{ex}};\omega)$ are given by

$$\begin{aligned}V_{\mathbf{Q}_\parallel\mathbf{Q}'_\parallel}(z_{\mathrm{ex}},z_{\mathrm{pl}};\omega)=|\varphi_0|^2|d|^2\frac{Q_\parallel^2}{\varepsilon_0\varepsilon_2}G^{\mathrm{st}}_{\mathbf{Q}_\parallel}(z_{\mathrm{ex}},z_{\mathrm{pl}})\frac{Q'^2_\parallel}{\varepsilon_0\varepsilon_1}\\ \times\ G^{\mathrm{st}}_{\mathbf{Q}'_\parallel}(z_{\mathrm{pl}},z_{\mathrm{ex}})[\alpha_\parallel(\omega)\cos(\phi-\phi')\\ +\ \alpha_z(\omega)],\end{aligned} \tag{16}$$

$$\begin{aligned}S_{\mathbf{Q}_\parallel}(z_{\mathrm{ex}},z_{\mathrm{pl}};\omega)=\frac{Q_\parallel^2}{\varepsilon_0\varepsilon_2}G^{\mathrm{st}}_{\mathbf{Q}_\parallel}(z_{\mathrm{ex}},z_{\mathrm{pl}})\\ \times\ [\alpha_\parallel(\omega)E_0^V(\mathbf{r}_{\mathrm{pl}};\omega)-i\alpha_z(\omega)E_0^z(\mathbf{r}_{\mathrm{pl}};\omega)].\end{aligned} \tag{17}$$

The first of the two terms, $V_{\mathbf{Q}_\parallel\mathbf{Q}'_\parallel}$, describes effects of the effective exciton-exciton interaction mediated by the plasmonic nanoparticle. This has the form of coupling between induced dipoles, as apparent from the characteristic cosine dependence on the relative angle $\phi-\phi'$. In the following, it is interpreted as an additional potential for the center-of-mass motion of the excitons. Due to the symmetry of the system, we chose $\alpha_\parallel=\alpha_x=\alpha_y$. The term on the right-hand side, $S_{\mathbf{Q}_\parallel}(z_{\mathrm{ex}},z_{\mathrm{pl}};\omega)$, represents the excitation caused by the external electric field. This excitation is initially scattered and enhanced by the AuNP before coupling to the TMDC. The interaction mediated via the in-plane and the z axis of the AuNP, respectively, is qualitatively different, as can be seen from the additional imaginary unit in front of the z component.

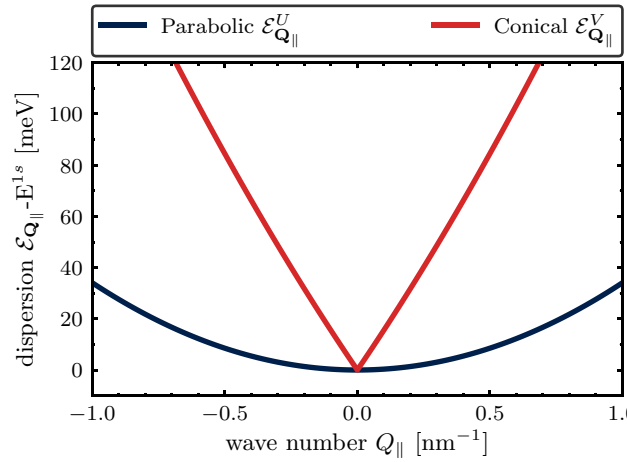

FIG. 2. *Dispersion.* The exchange coupling causes a split in the dispersion, resulting in parabolic dispersion for the noninteracting $p^U_{\mathbf{Q}_\parallel}$, and a conical dispersion for $p^V_{\mathbf{Q}_\parallel}$, which experiences interaction with the gold nanoparticle. The distinctive shape of the dispersion has also influenced its nomenclature.

In agreement with Ref. [61], we show in Fig. 2 that the exchange coupling in Eq. (14) leads to the formation of a parabolic lower band and a conical upper band in the excitonic dispersion. For this reason, we have chosen U and V as indices for the parabolic and conical dispersion, respectively. We define their dispersion from

$$\mathcal{E}^U_{\mathbf{Q}_\parallel}=E^{1s}+\frac{\hbar^2\mathbf{Q}_\parallel^2}{2M}, \tag{18}$$

$$\mathcal{E}^V_{\mathbf{Q}_\parallel}=E^{1s}+\frac{\hbar^2\mathbf{Q}_\parallel^2}{2M}+X_{\mathbf{Q}_\parallel}(z_{\mathrm{ex}}). \tag{19}$$

The pronounced splitting observed in U and V branches, as shown in Fig. 2, is facilitated by the reduced screening effect in TMDC monolayers compared with conventional quantum wells [76] through enhanced binding energy and exchange coupling.

Summarizing our analytical advances so far, we use a diagonalization [61] that reorients the wave-number coordinate system in the direction of $\mathbf{Q}_\parallel$ and perpendicular to it in Eq. (12). Therefore, this diagonalization with respect to the exchange coupling of K or K' valley can effectively be seen as a diagonalization in transverse and longitudinal components with respect to the wave vector $\mathbf{Q}_\parallel$ orientation and leads to the emergence of two distinct branches (U and V): We find one branch, where the exchange coupling contributions compensate one another and result in an effectively undisturbed parabolic excitonic dispersion (U branch). The other branch (V branch) contains contributions from valley exchange coupling. For the V branch, for small $\mathbf{Q}_\parallel$, the linear dependence on the momentum $|\mathbf{Q}_\parallel|$ (Taylor expansion) dominates and results in the noticeable effective splitting of the dispersion in Fig. 2 for $\mathbf{Q}_\parallel\neq 0$. Including the contributions from the AuNP, we find that only one of the TMDC exciton components (V branch), Eq. (14), is coupled to the AuNP, while the other

component (U branch) in Eq. (13), is completely decoupled from the AuNP and resembles the undisturbed excitonic case in Eq. (1).

III. PLEXCITONIC STATES

Similar to identifying the Wannier equation in the semiconductor Bloch equation [60,76,77] which captures the relative motion of electron and hole, we identify an eigenvalue equation in the conical Bloch equation, Eq. (14). This eigenvalue equation captures the modification of the dispersion due to exchange coupling as well as the interaction of AuNP plasmon and TMDC excitons and describes the full excitonic center-of-mass motion with in-plane momentum $\mathbf{Q}_\parallel$:

$$\left[\frac{\hbar^2\mathbf{Q}_\parallel^2}{2M} + X_{\mathbf{Q}_\parallel}(z_{\mathrm{ex}})\right]\Psi^{\mathrm{R},\lambda}_{\mathbf{Q}_\parallel} - \frac{1}{(2\pi)^2}\int \mathrm{d}^2\mathbf{Q}'_\parallel \times V_{\mathbf{Q}_\parallel\mathbf{Q}'_\parallel}(z_{\mathrm{ex}}, z_{\mathrm{pl}};\omega)\,\Psi^{\mathrm{R},\lambda}_{\mathbf{Q}'_\parallel} = E^\lambda \Psi^{\mathrm{R},\lambda}_{\mathbf{Q}_\parallel}, \tag{20}$$

The nonlocal plasmon-induced potential $V_{\mathbf{Q}_\parallel\mathbf{Q}'_\parallel}$ determines the center-of-mass motion $\mathbf{Q}_\parallel$ on the dispersion modified by the exchange coupling [left side of Eq. (20)]. Although the Wannier equation and the plexcitonic eigenvalue equation, Eq. (20), which we treat as a Schrödinger equation, share formal similarities, they differ qualitatively because the plasmon-induced potential $V_{\mathbf{Q}_\parallel\mathbf{Q}'_\parallel}$ is complex due to the complex-valued polarizability $\boldsymbol{\alpha}(\omega)$, cf. Eq. (16).

Accordingly, the eigenvalue equation, Eq. (20), becomes non-Hermitian which results in complex-valued eigenvalues and requires to distinguish left and right eigenvectors $\Psi^{\mathrm{L},\lambda}_{\mathbf{Q}'_\parallel}$ and $\Psi^{\mathrm{R},\lambda}_{\mathbf{Q}'_\parallel}$ [78,79] as will be done in Sec. III B. We refer to these new eigenstates as *plexcitonic states* because they describe the hybridized plasmon-exciton states of plasmonic and excitonic character.

In this section, we study the eigenvalue equation numerically and analyze the eigenvalues and eigenvectors in detail which we use in subsequent sections to define macroscopic quantities. For this purpose, we choose an oblate spheroid as depicted in Fig. 1. The explicit parameters can be found in Table I.

A. Eigenvalues of hybrid structure

The eigenvalue analysis of Eq. (20) by numerical eigendecomposition in analogy to established methods for the Wannier equation [55,80] reveals a finite number of eigenvalues with negative real part representing bound states (discussion below). The eigenvalues with positive real part distribute quasicontinuously along $\mathcal{E}^{U/V}_{\mathbf{Q}_\parallel}$. Figure 2 shows the dispersion: $\mathcal{E}^{V}_{\mathbf{Q}_\parallel}$ is conical for the parameter range of interest, consistent with recent work [61]. For increasing background permittivity ε_2, the dispersion interpolates between a cone and a parabola. Further discussion on this behavior can be found in Appendix D 2.

Through a parameter study of the background permittivities ε_1 and ε_2, the aspect ratio of the ellipsoid r_{xy}/r_z, and the distance between AuNP and TMDC $|z_{\mathrm{pl}} - z_{\mathrm{ex}}|$, we observe up to three eigenvalues with negative real part up to 100 meV

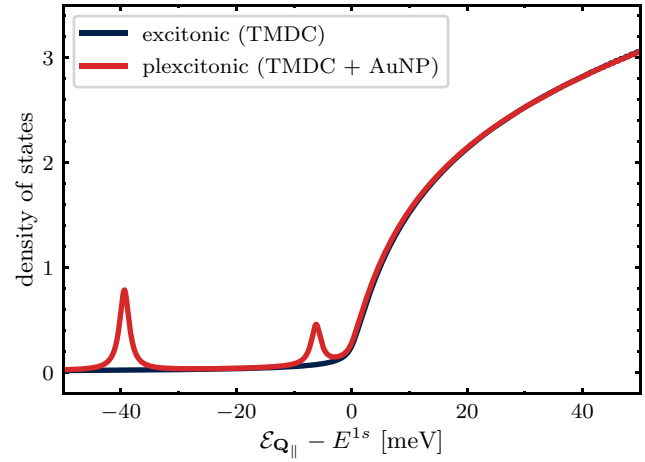

FIG. 3. *Excitonic density of states.* Comparison of the excitonic density of states for the interacting plexcitonic and the purely excitonic system where the potential $V_{\mathbf{Q}_\parallel\mathbf{Q}'_\parallel}$ in Eq. (20) was set to zero artificially for a spheroid with $r_{xy} = 8$ nm and $r_z = 4$ nm. The plexcitonic plot exhibits two additional peaks at negative energy, corresponding to the coupling via the in-plane component $\alpha_\parallel$ of the AuNP, with a multiplicity of two, and the z component α_z with a multiplicity of one. The peak at ≈ -39 meV corresponds to the in-plane coupling, while the one at ≈ -8 meV is caused the interaction via the z component. For the graphical representation, we used $\gamma_\ell = 1$ meV .

as well as associated eigenvectors (discussion below). The imaginary contribution (broadening in the spectrum) is on the same order of magnitude. These eigenvalues correspond to an attractive interaction mediated by the plasmon-induced potential $V_{\mathbf{Q}_\parallel\mathbf{Q}'_\parallel}$ in Eq. (20) that spatially localize excitons. We found that each of these eigenvalues originates from the interaction with the plasmonic mode along one of the three Cartesian axes of the nanoparticle. The frequency dependence of the binding energies is discussed in Appendix D 2. To illustrate these results, we calculate the excitonic density of states (DOS),

$$\mathrm{DOS}(E) = \frac{1}{A}\sum_\lambda \delta(E - E^\lambda), \tag{21}$$

by evaluating the Dirac delta distribution $\delta(E - E^\lambda)$ for the real part of the eigenvalues only. To be able to plot the DOS, we approximate the delta distribution with Lorentzian functions $\mathcal{L}_{\gamma_\ell}(E, E^\lambda)$, which introduces an artificial linewidth γ_ℓ. The introduced linewidth γ_ℓ serves the visual purpose of presentation of the numerically observed dense continuum states and the discrete states at negative energy compared with the $1s$ exciton resonance and should not be interpreted as a physical quantity.

Using $\gamma_\ell = 1$ meV, Fig. 3 shows that only the eigenvalues with negative real parts deviate from the quasicontinuous spectrum. By switching the interaction with the external particle on and off in our numerical implementation, we can compare the purely excitonic system to the interacting plexcitonic one that includes the effective exciton-exciton interaction $V_{\mathbf{Q}_\parallel\mathbf{Q}'_\parallel}$, mediated via the plasmonic nanoparticle. For our choice of parameters (oblate spheroid), cf. Table I, we find

two interaction-induced peaks at negative energies that results in a nonvanishing density of states at the respective eigenvalue energy. Due to the symmetry of the spheroid, we find that the eigenvalues corresponding to the interaction via the in-plane axes are degenerate and cause the peak at -39 meV, while the peak at -8 meV originates from interaction via the out-of-plane AuNP axis. A detailed parameter study for which parameters we obtain negative eigenvalues and localized eigenstates is provided in Appendix D.

Figure 3 displays the excitonic DOS for the conical excitonic dispersion without interaction with the nanoparticle, represented by the blue line. The real and positive eigenvalues are quasicontinuously distributed among the dispersion $\mathcal{E}^V_{\mathbf{Q}_\parallel}$. In contrast with strictly two-dimensional systems with parabolic dispersion, the DOS is not a step function due to the presence of a linear term in the dispersion relation, cf. Eq. (19), that depends on the center-of-mass momentum $\mathbf{Q}_\parallel$.

For the plexcitonic case (red), a numerical analysis shows that all eigenvalues with positive real part distribute on the conical dispersion and have negligible imaginary parts (on the order of the numerical accuracy). However, the eigenvalues with negative real part deviate significantly from the conical excitonic case, as seen in Fig. 3, and have non-negligible imaginary parts. The imaginary parts of the eigenvalues originate from nature of the lossy plasmon resonance and Förster-type processes between TMDC exciton and AuNP plasmon and introduce additional dephasing channels [12,14].

Based on our findings, we can conclude that the plasmon-mediated exciton-exciton interaction leads to the formation of plexcitonic states, exhibiting negative real part of the eigenvalue. We interpret this feature as the formation of bound states, where the real part of the eigenvalue represents the binding energy. These states cause the deviation in the density of states from the conical excitonic case in Fig. 3.

B. Eigenvectors and probability density

In this section, we analyze the eigenvectors corresponding to the negative eigenvalues presented in the previous section. In the usual excitonic picture, solutions of the Wannier equation [57] describe the relative electron-hole motion and their wave functions represent the probability amplitudes of their motion.

Due to its non-Hermitian nature, the physical interpretation of the plexcitonic eigenvalue equation is not straightforward. It generates left and right eigenvectors $\Psi^{L,\lambda}_{\mathbf{Q}_\parallel}$, $\Psi^{R,\lambda}_{\mathbf{Q}_\parallel}$. To address this issue, and to calculate observables, we follow the approach presented in Ref. [81] and define the complex-valued probability density,

$$\rho^\lambda(\mathbf{r}_\parallel) \equiv \Psi^{L,\lambda}(\mathbf{r}_\parallel)\Psi^{R,\lambda}(\mathbf{r}_\parallel), \tag{22}$$

where we use a normalization scheme:

$$\left\langle \Psi^{L,\lambda}_{\mathbf{Q}_\parallel} | \Psi^{R,\mu}_{\mathbf{Q}_\parallel} \right\rangle = \delta^{\lambda\mu}, \tag{23}$$

for the left and right eigenvectors $\Psi^{L,\lambda}_{\mathbf{Q}_\parallel}$, $\Psi^{R,\lambda}_{\mathbf{Q}_\parallel}$ with the scalar product defined as a 2D momentum integral over $\mathbf{Q}_\parallel$.

We further normalize the real-space probability density $\rho^\lambda(\mathbf{r}_\parallel)$, ensuring its real part integrates to one while its imaginary component vanishes when integrated over space. Within the scope of this work, the real component is associated with a probability distribution, while the interpretation of the imaginary component is open but both parts need to be considered in the calculation of observables.

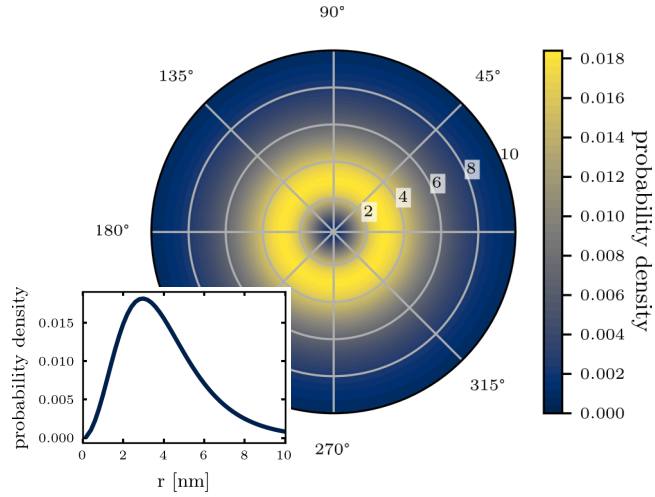

FIG. 4. *Probability density in real space.* The eigenvalues corresponding to in-plane interaction are degenerate, here we plot the superposition of the two probability densities corresponding to this attractive in-plane interaction. The inset shows the radial profile of the probability density.

Our analysis reveals that the eigenvectors $\Psi^{L,\lambda}_{\mathbf{Q}_\parallel}$ and $\Psi^{R,\lambda}_{\mathbf{Q}_\parallel}$, respectively, belonging to the three negative eigenvalues (bound states), correspond to the degeneracy of the spatial axes of the gold nanoparticle polarizability $\boldsymbol{\alpha}(\omega)$. They accurately reflect the symmetry of the coupling axis, showing either an x or y orientation or a radial symmetry for coupling via the out-of-plane component. As expected, we observe that these eigenvectors related to negative eigenvalues are localized near the origin, thus representing bound states, while the eigenvectors corresponding to positive eigenvalues are spread out throughout momentum space and represent the discretization of the considered Hilbert space. Therefore, the AuNP allows us to study exciton localization in the vicinity of the AuNP. To illustrate this, we discuss the real-space probability density $\rho^\lambda(\mathbf{r}_\parallel)$, defined in Eq. (22). In Fig. 4, we plot the real part of the sum of the probability densities, cf. Eq. (22), associated with the degenerate eigenvalue from the in-plane coupling, resulting in a ring-shaped distribution around the origin. The x and y components individually exhibit orientation along their respective axes.

The ring-shaped feature is a result of the in-plane dipole-dipole interaction between the spatially fixed dipole (plasmon) and the dipole that is free to move in a 2D plane (exciton). The interaction that results from dipole-dipole interaction via the z component of the plasmon is studied in Appendix D 4.

In summary, we find that the additional states in the density of states reveal negative eigenenergies, cf. Fig. 3. These states are spatially confined near the gold nanoparticle, indicating that they correspond to bound states. In Secs. IV and V, we analyze the implications of these states on macroscopic observables such as the macroscopic TMDC polarization and the electric near-field in more detail.

IV. LOCALIZATION

In this section, we analyze the impact of the external nanoparticle on the macroscopic polarization within the TMDC layer, contributing to optical observables via Maxwell's equations. As a macroscopic observable, we use the absolute value of the TMDC polarization in Eq. (2), that we map on the plexcitonic eigenstates defined by Eq. (20), using the plexcitonic expansion

$$p^V_{\mathbf{Q}_\parallel}(\omega) = \sum_\lambda \Psi^{R,\lambda}_{\mathbf{Q}_\parallel}\, p^\lambda(\omega), \tag{24}$$

with suitable expansion coefficients p^λ. We expand Eq. (14) using the plexcitonic expansion in Eq. (24), expressing it in terms of right eigenvectors $\Psi^{R,\lambda}_{\mathbf{Q}_\parallel}$ which form a complete basis in momentum space. We then project this expanded equation onto the corresponding left eigenvectors $\Psi^{L,\lambda}_{\mathbf{Q}_\parallel}$ and utilize the biorthonormality relation [see Eq. (23)].

This approach yields a dynamical equation for the expansion coefficient p^λ, which we term the *plexcitonic polarization equation*:

$$p^\lambda(\omega) = \frac{d^* \varphi_0^*}{(2\pi)^2} \int \mathrm{d}^2\mathbf{Q}'_\parallel \frac{\left(\Psi^{L,\lambda}_{\mathbf{Q}'_\parallel}\right)^* \left(E^{0,V}_{\mathbf{Q}'_\parallel}(z_{\mathrm{ex}}) + S_{\mathbf{Q}'_\parallel}\right)}{E^{1s} + E^\lambda - \hbar\omega - i\gamma}. \tag{25}$$

We observe that the plexcitonic polarization p^λ can be excited by two external source terms: the external field at the position of the TMDC, $E^{0,V}_{\mathbf{Q}'_\parallel}(z_{\mathrm{ex}})$, and the field scattered by the AuNP, $S_{\mathbf{Q}'_\parallel}$, as described in Eq. (17). The latter carries a nonvanishing in-plane momentum $\mathbf{Q}_\parallel$. To simplify the notation, we no longer explicitly mention the dependencies of $S_{\mathbf{Q}'_\parallel}$. Notably, the complex-valued plexcitonic eigenvalues E^λ renormalize not only the resonance energy, as seen in the denominator, but also the dephasing of the nanostructure, through their imaginary part which are negative and thus increase the effective dephasing of the nanostructure.

By Fourier transformation of Eq. (2), we find that the macroscopic TMDC polarization, including all contributions from $p^U_{\mathbf{Q}_\parallel}(\omega)$ and $p^V_{\mathbf{Q}_\parallel}(\omega)$, can be written as

$$\begin{aligned}
\mathbf{P}^{\pm}_{\mathrm{TMDC}}(\mathbf{r};\,\omega) = \frac{|d|^2|\varphi_0|^2}{2}\frac{1}{(2\pi)^2}\int \mathrm{d}^2\mathbf{Q}_\parallel \Bigg\{ e^{i\mathbf{Q}_\parallel\cdot\mathbf{r}_\parallel}\Bigg[&\frac{1}{E^{1s} + \frac{\hbar^2\mathbf{Q}_\parallel^2}{2M} - \hbar\omega - i\gamma}\begin{pmatrix} 1 & -e^{-2i\phi} \\ -e^{2i\phi} & 1 \end{pmatrix}\cdot \mathbf{E}^{0,\pm}_{\mathbf{Q}_\parallel}(z_{\mathrm{ex}}) \\
&+ \frac{1}{(2\pi)^2}\int \mathrm{d}^2\mathbf{Q}'_\parallel \sum_\lambda \frac{\Psi^{R,\lambda}_{\mathbf{Q}_\parallel}\left(\Psi^{L,\lambda}_{\mathbf{Q}'_\parallel}\right)^*}{E^{1s} + E^\lambda - \hbar\omega - i\gamma}\begin{pmatrix} e^{-i\phi}e^{i\phi'} & e^{-i\phi}e^{-i\phi'} \\ e^{i\phi}e^{i\phi'} & e^{i\phi}e^{-i\phi'} \end{pmatrix}\cdot \mathbf{E}^{0,\pm}_{\mathbf{Q}'_\parallel}(z_{\mathrm{ex}}) \\
&+ \frac{1}{(2\pi)^2}\int \mathrm{d}^2\mathbf{Q}'_\parallel \sum_\lambda \frac{Q_\parallel^2}{\varepsilon_0\varepsilon_2}\frac{\Psi^{R,\lambda}_{\mathbf{Q}_\parallel}\left(\Psi^{L,\lambda}_{\mathbf{Q}'_\parallel}\right)^* G^{\mathrm{st}}_{\mathbf{Q}_\parallel}}{E^{1s} + E^\lambda - \hbar\omega - i\gamma}\begin{pmatrix} e^{-i\phi}e^{i\phi'} & e^{-i\phi}e^{-i\phi'} & -e^{-i\phi} \\ e^{i\phi}e^{i\phi'} & e^{i\phi}e^{-i\phi'} & -e^{i\phi} \end{pmatrix}\cdot \begin{pmatrix} \alpha_\parallel E_0^+(\mathbf{r}_{\mathrm{pl}}) \\ \alpha_\parallel E_0^-(\mathbf{r}_{\mathrm{pl}}) \\ i\sqrt{2}\,\alpha_z E_0^z(\mathbf{r}_{\mathrm{pl}}) \end{pmatrix}\Bigg] + \mathrm{c.c.}\Bigg\}.
\end{aligned} \tag{26}$$

In Eq. (26), we can identify three distinct contributions to the macroscopic TMDC polarization. The first term corresponds to half the unperturbed response of the TMDC, which is independent of any interaction with the AuNP. The second term captures the interaction between the TMDC and the AuNP, as well as the TMDC self-interaction which is described by the plexcitonic eigenvalues E^λ and eigenvectors $\Psi^{L,\lambda}_{\mathbf{Q}_\parallel}$ and $\Psi^{R,\lambda}_{\mathbf{Q}_\parallel}$. The third term represents the external electric field scattered and enhanced by the AuNP and subsequently transferred to the TMDC position where it contributes to the TMDC polarization. In the limit of vanishing AuNP, the third term vanishes and the second one reproduces the second half of the unperturbed TMDC response.

In Fig. 5, we plot the resulting macroscopic polarization of the TMDC from Eq. (26) when excited by a σ^+-polarized plane wave and find a radially symmetric distribution of the polarization around the nanoparticle location. According to Eq. (26), the spatial localization is mainly attributed to two key processes. The first one is the dipole-dipole interaction between the TMDC exciton and the AuNP plasmon, leading to the localized plexcitonic states discussed in Sec. III. The second one is the locally enhanced electric field in the TMDC layer, which occurs due to the scattering of the field by the AuNP. These processes are discussed individually in Appendix E 1.

This analysis reveals that proper selection of parameters, positioning a gold nanoparticle on a TMDC monolayer can induce the formation of plexcitonic states through dipole-dipole interactions. The resulting polarization enhancement in the TMDC underneath the nanoparticle effectively localizes carriers in the vicinity of the AuNP.

V. STRONG COUPLING

This section focuses on the study of the electric field emitted by the nanostructure in response to an external electric field. To calculate the electric field outside the nanostructure, we use the Green's method to solve the wave equation described in Eq. (6). We find for the electric field distribution surrounding the nanostructure:

$$\begin{aligned}
\mathbf{E}_{\mathbf{Q}_\parallel}(z;\,\omega) = &\mathcal{G}^{\mathrm{st}}_{\mathbf{Q}_\parallel}(z, z_{\mathrm{ex}})\cdot \mathbf{P}^{\mathrm{TMDC}}_{\mathbf{Q}_\parallel}(z_{\mathrm{ex}};\,\omega) \\
&+ \mathcal{G}^{\mathrm{st}}_{\mathbf{Q}_\parallel}(z, z_{\mathrm{pl}})\cdot \mathbf{P}^{\mathrm{AuNP}}_{\mathbf{Q}_\parallel}(z_{\mathrm{pl}};\,\omega) + \mathbf{E}^0_{\mathbf{Q}_\parallel}(z;\,\omega).
\end{aligned} \tag{27}$$

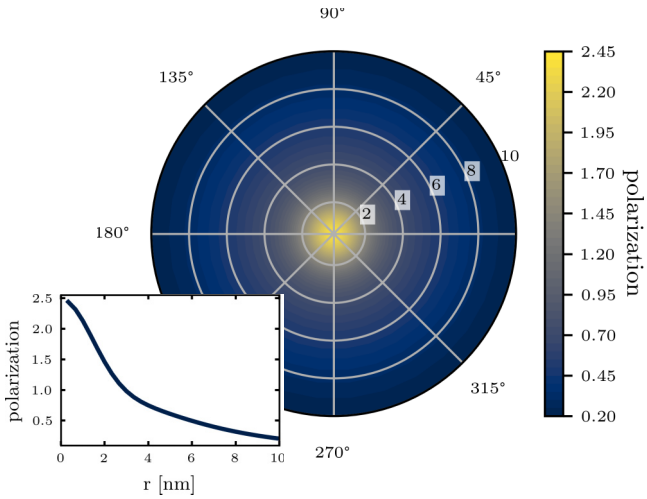

FIG. 5. *TMDC polarization in real space.* In the figure, we see for σ^+ excitation that full TMDC polarization localizes in a radially symmetric way below the metal nanoparticle.

The TMDC polarization is defined in Eq. (26) and the gold polarization can be found in Appendix E 2. Importantly, our analysis in Sec. II relies on the quasistatic approximation, which accurately describes the electric near-field where $\mathbf{Q}_\parallel \neq 0$ is dominant. Therefore, our analysis is limited to the electric near-field, which is well-captured by our approach. Note, that to accurately describe the electric far-field and account for radiative processes, it would be necessary to include the $\mathbf{Q}_\parallel = 0$ case in the calculation. Numerical evaluation of the electric near-field from Eq. (27) yields an optical near-field spectrum.

In Fig. 6, we plot the Fourier-transformed (purely real space) absolute value of the electric field intensity $|\mathbf{E}(\mathbf{r};\omega)|^2$

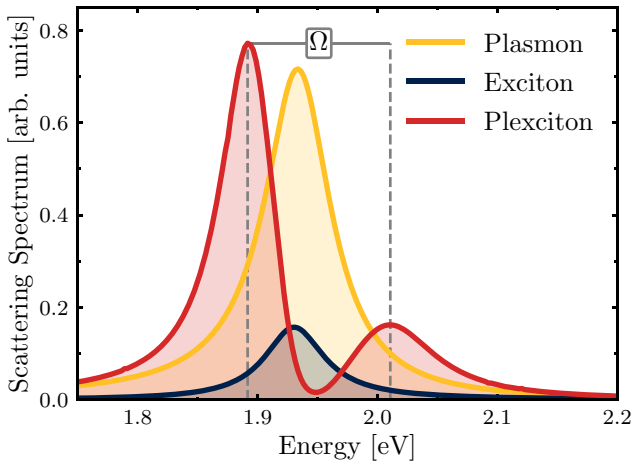

FIG. 6. *Peak splitting*. For comparable excitonic and plasmonic resonance energies, the response of the joint system splits into two distinct peaks at lower and higher energy compared with the shared resonance. The scattered electric field is detected at $x = 2\,\text{nm}$, $y = 0\,\text{nm}$, and $z = -5\,\text{nm}$. The excitonic resonance energy is $E^{1s} = 1.93\,\text{eV}$, other parameters for room temperature can be found in Table I. The plasmonic and plexcitonic spectra are presented in the correct ratio, the excitonic spectrum is scaled for display in the same plot.

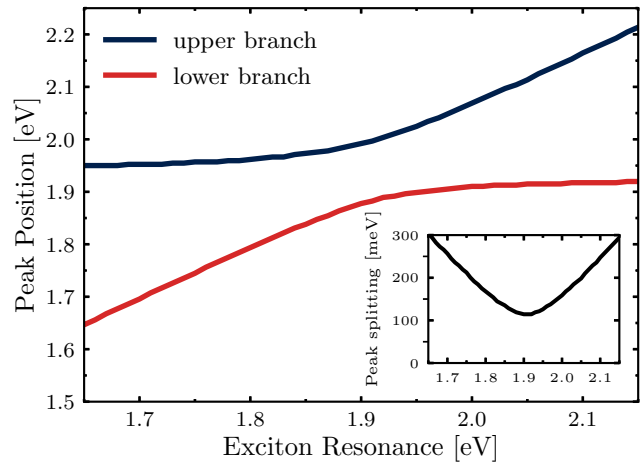

FIG. 7. *Avoided crossing*. Numerically tuning the excitonic resonance allows investigating the peak splitting in the plexcitonic spectrum and shows the avoided crossing behavior of the system, indicating a strong-coupling regime. The given spectrum displays the peak positions, cf. Fig. 6, over a wide exciton resonance range. The inset illustrates the peak separation with its lowest value being the Rabi splitting that is approximately 110 meV in this case. All parameters used in the numerical implementation can be found in Table I.

for excitation by plane waves. In contrast with TMDC excitation with a plane wave that only has a vanishing in-plane momentum, scattering off the AuNP generates electric field components in the near-field that possess a nonvanishing center-of-mass momentum $\mathbf{Q}_\parallel \neq 0$. These components can interact with momentum-dark excitonic states $\mathbf{Q}_\parallel \neq 0$ in the TMDC illustrating that the observed features result from dark excitons. The spectra in Fig. 6 show that the individual noninteracting energy transitions of TMDC exciton and AuNP plasmon are designed so that their respective resonances, excitonic and plasmonic, occur at the same spectral location, cf. Table I, as depicted in the individual plasmon and exciton plots presented in Fig. 1. However, for both systems in contact we observe spectral peak splitting, which is a sign of strong coupling between the individual TMDC exciton and AuNP plasmon oscillators [49,50]. Since our description relies on the excitation of dark excitons in the near-field, we attribute the occurrence of strong coupling to the spatial localization of near-field excited dark excitons.

We also highlight that our numerical approach allows us to artificially tune the excitonic resonance while keeping the plasmonic resonance fixed. Figure 7 shows the two peak positions with varying $1s$ excitonic resonance. Resonance energies far from each other have little influence on one another, while we observe a significant peak splitting once the spectral separation of their peaks approaches their linewidths. Compared with the uncoupled case, the interaction leads to a minimum value of the spectral splitting of the observed spectral peaks, which we call effective Rabi splitting. This can be interpreted as avoided crossing behavior and supports the finding that the system behaves in a strong-coupling regime.

Experimentally observed effective spectral Rabi splittings are in the same range, i.e., 50–150 meV, as predicted by our parameter-free description. This is a very reasonable result

compared with the very different ranges of Rabi splittings on the order of 100 μeV [82–84] occurring in atomic systems and offers a justification for the used approximations.

VI. CONCLUSION AND PERSPECTIVES

We have presented a self-consistent theoretical approach for the near-field optical interaction between a monolayer of TMDC and a gold nanoparticle. Starting from the excitonic and plasmonic picture, we identified a novel eigenvalue equation that describes the center-of-mass motion of the excitons in an effective potential that features hybridized exciton-plasmon states. In this context, strong coupling is related to the excitation of momentum-dark excitons and their spatial localization in the monolayer near the AuNP: the density of states contains bound states below the excitonic $1s$ resonance. This interpretation is supported by the plexcitonic probability density and its influence on the spectral and spatial properties of the macroscopic TMDC polarization.

Our analysis shows that the strong localization near the external particle leads to a strong coupling behavior visible in the electric near-field. Through a detailed parameter study, we establish a connection between the existence of these common states and an avoided crossing behavior in the spectral representation of the system. Our findings provide evidence that metal nanoparticles can be used to effectively localize excitons in two-dimensional TMDC layers.

ACKNOWLEDGMENTS

We acknowledge fruitful discussions with Chelsea Carlson (Queen's University) as well as Manuel Katzer, Dominik Christiansen, and Jonas Grumm (TU Berlin). This work is supported financially by the Deutsche Forschungsgemeinschaft (DFG) through Project KN 427/14-1 (Project No. 420760124), through Project SE 3098/1-1 (Project No. 432266622), and SFB 951 (Project No. 182087777). We also acknowledge support from the Natural Sciences and Engineering Research Council of Canada, and the Alexander von Humboldt Foundation through a Humboldt Research Award.

The authors have no conflicts of interest to disclose.

APPENDIX A: ANALYTICAL MODEL OF THE OPTICAL RESPONSE OF A GOLD NANOPARTICLE

We model the gold permittivity $\varepsilon_{\mathrm{Au}}(\omega)$ using the analytical expression provided in Ref. [51]. It reads

$$\varepsilon_{\mathrm{Au}}(\omega) = \varepsilon_\infty - \frac{\omega_p^2}{\omega(\omega + i\gamma_p)} + \sum_{j=1,2} A_j \omega_j \left[\frac{e^{i\varphi_j}}{\omega_j - \omega - i\gamma_j} + \frac{e^{-i\varphi_j}}{\omega_i + \omega + i\gamma_j} \right], \tag{A1}$$

where the first two terms describe a standard Drude model and the last terms additional interband transitions at the respective energies. The parameter values are given in Table I and were obtained by the authors of Ref. [51] as fits to the experimental data in Ref. [62].

To incorporate the geometry of the nanoparticle, we employ Mie-Gans theory [52,53] as we allow the AuNP to be spheroidal and obtain the AuNP polarizability given in Eq. (3). The impact of the aspect ratio is contained in the depolarization factors L_i, which change the optical response via the respective semi-axes,

$$L_x = L_y = \frac{1}{2e_0^2}\left(\frac{\sqrt{1-e_0^2}}{e_0} \arcsin(e_0) - \left(1 - e_0^2\right) \right), \tag{A2}$$

$$\text{and} \quad L_z = \frac{1}{e_0^2}\left(1 - \frac{\sqrt{1-e_0^2}}{e_0} \arcsin(e_0) \right). \tag{A3}$$

For the oblate spheroid the x and y component coincide due to symmetry. The eccentricity e_0 is defined to be

$$e_0 = 1 - \frac{r_z^2}{r_{xy}^2}, \tag{A4}$$

and features the lengths of the semi-axes r_i.

APPENDIX B: SCREENED POTENTIAL

For our model structure, we use a Rytova-Keldysh-type approach [6,7] in order to calculate the potential that is later used in the Wannier equation in order to incorporate substrate effects on the carrier localization. The potential for our effective four-layer system of ε_1-ε_2-TMDC-ε_2 reads

$$V_{\mathbf{k}} = \frac{q}{2\varepsilon_0 \tilde{\varepsilon} k} \frac{e^{2kL} + e^{kL}(\delta_{\tilde{\varepsilon},\varepsilon_2} + \delta_{\tilde{\varepsilon},\varepsilon_2,\varepsilon_1}) + \delta_{\tilde{\varepsilon},\varepsilon_2}\delta_{\tilde{\varepsilon},\varepsilon_2,\varepsilon_1}}{e^{2kL} - \delta_{\tilde{\varepsilon},\varepsilon_2}\delta_{\tilde{\varepsilon},\varepsilon_2,\varepsilon_1}}, \tag{B1}$$

with the definitions

$$\delta_{\tilde{\varepsilon},\varepsilon_2} = \frac{\tilde{\varepsilon} - \varepsilon_2}{\tilde{\varepsilon} + \varepsilon_2}, \tag{B2}$$

$$\delta_{\tilde{\varepsilon},\varepsilon_2,\varepsilon_1} = \frac{\tilde{\varepsilon} - \varepsilon_2\xi}{\tilde{\varepsilon} + \varepsilon_2\xi}, \quad \xi = \frac{e^{2kR} - \delta_{\varepsilon_2,\varepsilon_1}}{e^{2kR} + \delta_{\varepsilon_2,\varepsilon_1}}, \tag{B3}$$

where L is the thickness of the TMDC layer and R is the thickness of the intermediate layer between the TMDC and the $z = 0$ plane, cf. Fig. 1.

APPENDIX C: GREEN'S FUNCTION

For our specific geometry depicted in Fig. 1, including the interface of two background permittivities ε_1 and ε_2 and assuming the TMDC to be effectively two dimensional, the Green's function can be calculated. We find, in agreement with Refs. [75,86],

$$G^{\mathrm{st}}_{\mathbf{Q}_\parallel}(z,z') = \begin{cases} -\frac{1}{2Q_\parallel} e^{-Q_\parallel|z-z'|} - \frac{1}{2Q_\parallel}\frac{\varepsilon_1-\varepsilon_2}{\varepsilon_1+\varepsilon_2} e^{-Q_\parallel|z+z'|}, & z,z' > 0 \\ -\frac{1}{Q_\parallel}\frac{\varepsilon(z)}{\varepsilon_1+\varepsilon_2} e^{-Q_\parallel|z-z'|}, & \mathrm{sgn}(z) \neq \mathrm{sgn}(z') \\ -\frac{1}{2Q_\parallel} e^{-Q_\parallel|z-z'|} - \frac{1}{2Q_\parallel}\frac{\varepsilon_2-\varepsilon_1}{\varepsilon_1+\varepsilon_2} e^{-Q_\parallel|z+z'|}, & z,z' < 0. \end{cases} \tag{C1}$$

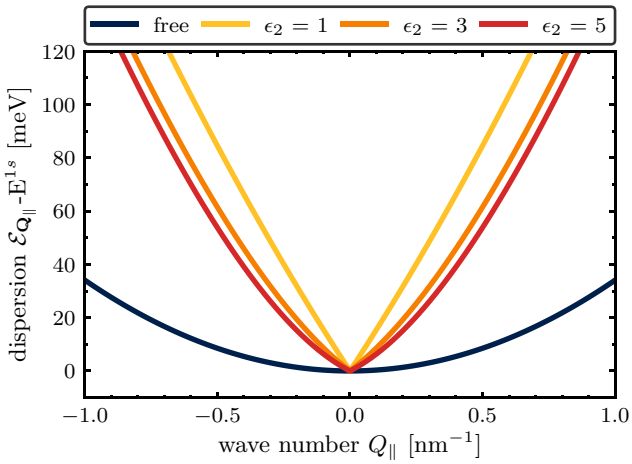

FIG. 8. *Dispersion relation*. The interacting dispersion $\mathcal{E}^V_{\mathbf{Q}_\parallel}$, cf. Eq. (19), is plotted for varying background permittivity ε_2 from yellow to red. One can see that the dispersion interpolates between linear and parabolic behavior. The free dispersion $\mathcal{E}^U_{\mathbf{Q}_\parallel}$ [cf. Eq. (18)] is plotted for reference in (dark) blue.

This Green's function is derived for the quasistatic case of $c \to \infty$ which is caused by the proximity of the AuNP and TMDC. Hence, to a good approximation, we can neglect radiative interactions. We find that the Green's function is defined piecewise depending on the position of the source z' and the observation location z.

APPENDIX D: EIGENSYSTEM

Our numerical implementation enables a comprehensive investigation of various parameter configurations for our system, which we explore in the following sections. First, we analyze the dispersion relation for varying background permittivity ε_2 in Sec. D 1. We then study the spectral eigenvalue distribution in Sec. D 2. In Sec. D 3, we analyze the dependence of the lowest eigenvalue on the nanoparticle aspect ratio

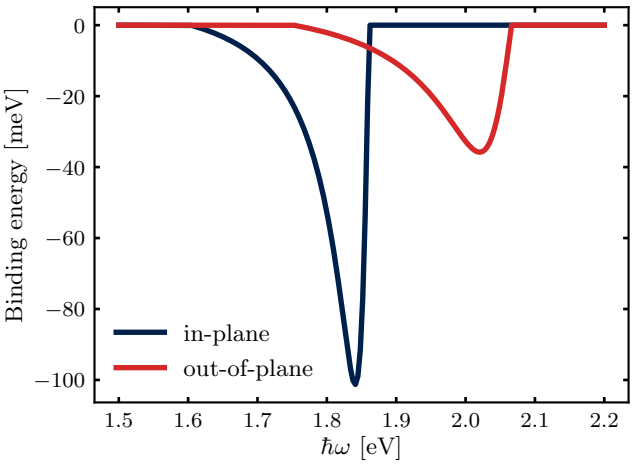

FIG. 9. *Lowest eigenvalues*. The lowest eigenvalue of the plexcitonic eigenvalue equation, cf. Eq. (20), highly depends on the choice of the spectral position of the excitonic 1*s* resonance. Here, the lowest eigenvalue for interacting via the in-plane or out-of-plane axis is given.

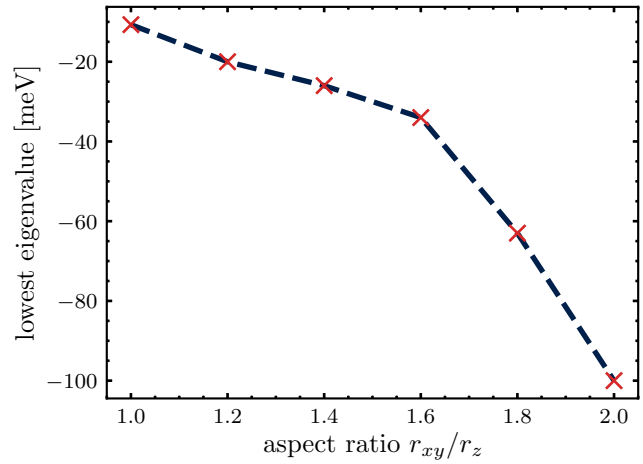

FIG. 10. *Influence of aspect ratio on lowest eigenvalue*. By varying the aspect ratio, we can adjust the effective distance between the AuNP and the TMDC layer for a fixed volume and thus modify the interaction strength. This plot displays the dependence of the lowest eigenvalue on the aspect ratio while maintaining a fixed volume.

to quantify the interaction strength. Finally, we investigate the corresponding eigenvectors (plexcitonic wave functions) in Sec. D 4.

1. Dispersion

The eigenvalues of the plexcitonic eigenvalue equation, Eq. (20), quasicontinuously distribute among the dispersion relation $\mathcal{E}^V_{\mathbf{Q}_\parallel}$. Only the negative eigenvalues differ from this distribution. Thus, we begin studying this dispersion relation for varying background permittivity ε_2 in Fig. 8. The purely excitonic dispersion $\mathcal{E}^U_{\mathbf{Q}_\parallel}$ is not affected by changing the background permittivity ε_2 while the plexcitonic dispersion $\mathcal{E}^V_{\mathbf{Q}_\parallel}$ is conical [61] for small ε_2 but becomes predominantly parabolic for larger ε_2.

2. Eigenvalues

In the following analysis, we examine the plexcitonic eigenvalues that deviate from the dispersion and become negative. This occurs when the TMDC exciton and AuNP plasmon are in resonance. Here, we focus on the distribution of the lowest eigenvalues, which we present in Fig. 9. Specifically, we explore two distinct distributions based on the interaction through the in-plane polarizability axis $\alpha_\parallel$ of the nanoparticle and the out-of-plane axis α_z.

As anticipated, one can clearly distinguish the distributions of eigenvalues resulting from in-plane and out-of-plane interaction, respectively. We observe spectral ranges where negative eigenvalues are absent, either due to interaction via a single axis or in a narrow spectral range for both axes. In the absence of negative eigenvalues, the individual components are out of resonance, which prevents attractive interactions. However, when the components are in resonance, we detect negative eigenvalues, which we interpret as the binding energy of the exciton in the potential induced by the AuNP. Notably, at certain spectral positions, these binding energies amount to several tens of meV.

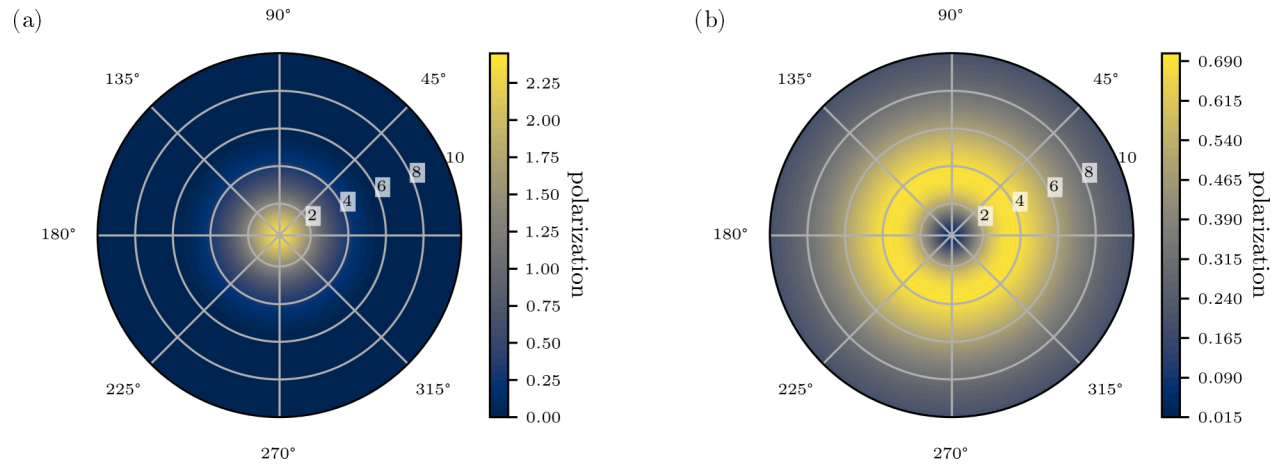

FIG. 11. *Macroscopic TMDC polarization.* We plot σ^+ polarization in panel (a) and σ^- polarization in panel (b) for the case of σ^+ excitation. In panel (a), the σ^+ contribution is centered around the origin, while in panel (b), the σ^- contribution forms a ring around the origin. The full polarization, shown in Fig. 5, is obtained as the sum of both contributions.

3. Au nanoparticle aspect ratio

In our numerical analysis presented in the main article, we consider spheroidal nanoparticles with an aspect ratio $r_{xy}/r_z = 2$. This choice of aspect ratio allows us to increase the nanoparticle volume while simultaneously decreasing the effective separation between the nanoparticle and TMDC layer. To investigate the influence of the aspect ratio r_{xy}/r_z on the coupling strength and quantify its effects, we recalculate the lowest eigenvalue for varying aspect ratio while keeping the nanoparticle volume fixed and position it right at the interface. The real part of the lowest eigenvalue as a function of aspect ratio is plotted in Fig. 10.

Our analysis shows that the binding strength increases as the aspect ratio of the spheroidal nanoparticle increases, resulting in a more negative lowest eigenvalue. This trend arises from the exponential dependence of the interaction strength on the separation, while the increase in volume with respect to the semi-axis in the out-of-plane direction is only linear. Therefore, we demonstrate that oblate spheroids exhibit a stronger interaction compared with a sphere of equal volume.

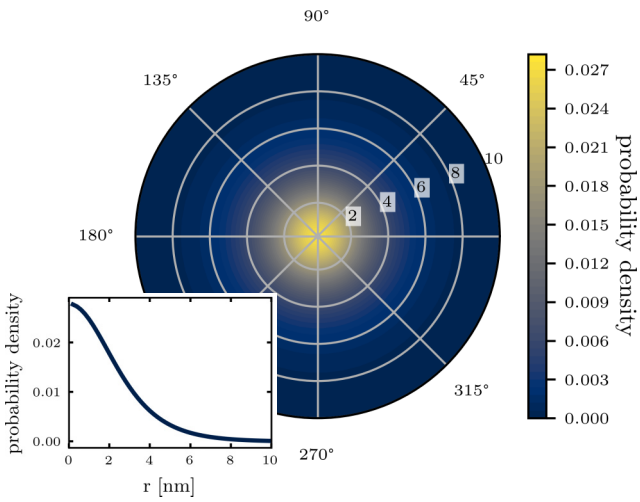

FIG. 12. *Probability density in real space.* Here, we plot the probability corresponding to interaction via the out-of-plane axis of the AuNP. The inset shows the radial profile of the probability density.

4. Eigenvectors

In Sec. III B, we presented the probability density resulting from interaction via the in-plane components of the AuNP. This probability density is ring-shaped around the origin due to dipole-dipole interaction. For completeness, we now provide the probability density corresponding to interaction via the out-of-plane component. In contrast with the probability density resulting from in-plane interaction, the probability density for out-of-plane interaction exhibits a Gaussian distribution centered around the origin of the AuNP position. This outcome can also be derived from the minimization of the dipole-dipole potential for dipoles that are perpendicular to one another.

APPENDIX E: MACROSCOPIC QUANTITIES

In this section, we shift our focus from the microscopic quantities discussed in the previous section to observable macroscopic quantities that can be derived from our calculations. Specifically, in Sec. E 1, we examine the circularly polarized components of the macroscopic TMDC polarization in real space. Additionally, in Sec. E 2, we provide an analytical expression for the AuNP polarization, which serves as a source in the Green's function approach used to calculate the electric field. In Sec. E 3, we analyze the parameter dependence of the Rabi splitting that was obtained in Sec. V.

1. Transition-metal dichalcogenide polarization

In Sec. IV, we presented the full TMDC polarization following excitation with a σ^+ pulse. In this section, we analyze the individual σ^+ or σ^- components of the polarization after excitation with a σ^+ pulse (see Fig. 11). The results are analogous for σ^- excitation.

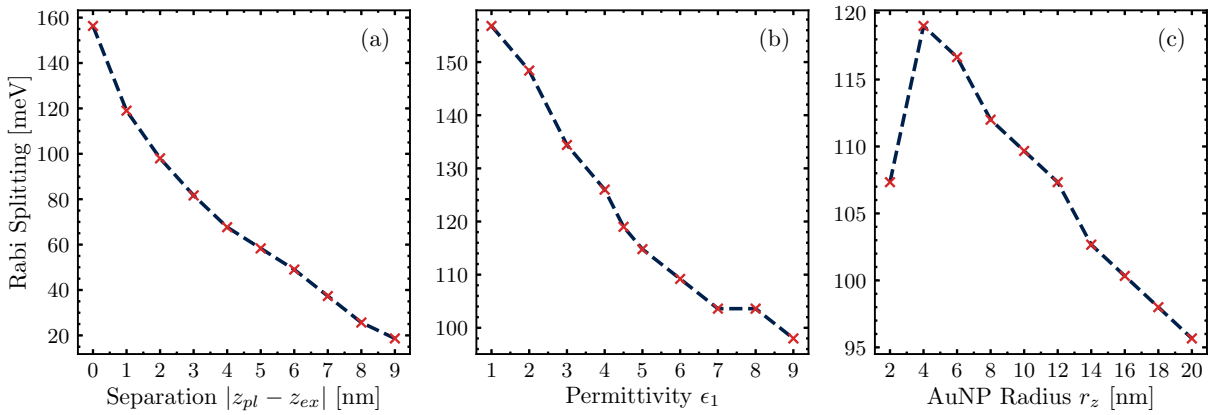

FIG. 13. *Rabi splitting*. The graphs display the dependence of the Rabi splitting over a parameter range that results in strong coupling. Panel (a) illustrates that an increase of the separation of TMDC and AuNP results in a decrease of the splitting. (b) For an increasing background permittivity ε_1 in the upper half space, the Rabi splitting decreases. (c) For an increasing AuNP radius r_z, the Rabi splitting reaches a maximum at ≈4 nm. This behavior qualitatively agrees with the dependence of the lowest eigenvalue on the AuNP radius.

Our analysis reveals two distinct shapes for the spatial distribution of the macroscopic TMDC polarization. The absolute value of the σ^+ polarization is Gaussian distributed and centered around the origin. For the absolute value of the σ^- polarization, a ring-shaped feature is observed, similar to the probability density investigated in Sec. III B, with vanishing polarization at the origin. These findings suggest that the selection rules are modified in the electric near-field [87], enabling the excitation of oppositely polarized light. Furthermore, we interpret our results as indicating that polarization of the same direction is primarily induced by the external field that scatters off the AuNP, whereas polarization of the opposite direction mostly originates from the dipole-dipole interaction between the TMDC exciton and AuNP plasmon, reproducing the shape of the probability density from Sec. III B.

2. Gold polarization

In Sec.V, we use Eq. (27) to propagate the material polarizations to the surroundings. This material polarization includes an effective polarization originating from the TMDC, whose Fourier-transformed version we provided in Eq. (26). Here, we provide the AuNP polarization in the mixed basis $(\mathbf{Q}_\parallel, z; \omega)$ (see Fig. 12), which is only defined at the spatial position of the AuNP,

$$\mathbf{P}^{\mathrm{AuNP},\pm}_{\mathbf{Q}_\parallel}(z_{\mathrm{pl}};\omega) = \frac{1}{(2\pi)^2}\int \mathrm{d}^2\mathbf{Q}'_\parallel \begin{pmatrix} \alpha_\parallel E^+_{\mathbf{Q}'_\parallel}(z_{\mathrm{pl}}) \\ \alpha_\parallel E^-_{\mathbf{Q}'_\parallel}(z_{\mathrm{pl}}) \\ \alpha_z E^z_{\mathbf{Q}'_\parallel}(z_{\mathrm{pl}}) \end{pmatrix} + \frac{|d|^2|\varphi_0|^2}{2}\sum_\lambda \frac{1}{E+E^\lambda-\hbar\omega-i\gamma}\frac{1}{(2\pi)^2}$$
$$\times \int \mathrm{d}^2\mathbf{Q}'_\parallel \psi^R_{\mathbf{Q}'_\parallel}\frac{{Q'_\parallel}^2}{\varepsilon_0\varepsilon_1}G^{\mathrm{st}}_{\mathbf{Q}'_\parallel}(z_{\mathrm{pl}},z_{\mathrm{ex}})\begin{pmatrix} e^{-i\phi'}\alpha_\parallel \\ e^{i\phi'}\alpha_\parallel \\ i\alpha_z \end{pmatrix}\frac{\alpha_\parallel}{(2\pi)^2}\int \mathrm{d}^2\mathbf{Q}''_\parallel \left(\psi^L_{\mathbf{Q}''_\parallel}\right)^*\Big[(e^{i\phi''}E^+_{\mathbf{Q}''_\parallel}(z_{\mathrm{ex}}) + e^{-i\phi''}E^-_{\mathbf{Q}''_\parallel}(z_{\mathrm{ex}}))$$
$$+\frac{Q^2_\parallel}{\varepsilon_0\varepsilon_2}G^{\mathrm{st}}_{\mathbf{Q}''_\parallel}(z_{\mathrm{ex}},z_{\mathrm{pl}})(e^{i\phi''}E^+(\mathbf{r}_{\mathrm{pl}}) + e^{-i\phi''}E^-(\mathbf{r}_{\mathrm{pl}}))\Big]. \tag{E1}$$

The polarization of the system is composed of three contributions. The first one is the dipole response of the AuNP, which is determined by its polarizability $\boldsymbol{\alpha}$ and the external electric field at the AuNP position $\mathbf{E}_{\mathbf{Q}'_\parallel}(z_{\mathrm{pl}})$. The second contribution arises from the interaction of the external electric field with the TMDC layer, which is then mediated to the AuNP. The third contribution arises from the effective self-interaction of the plasmon, mediated via the TMDC layer.

3. Rabi splitting

In Fig. 7, we observed that our system reveals a Rabi splitting of several tens of meV and thus clearly operates in the strong-coupling regime. The Rabi splitting can be tuned via various system parameters, which we analyze individually to understand their impact on Ω in Fig. 13.

In our study, we observe a decrease in the Rabi splitting as the TMDC or AuNP spacing decreases, consistent with the findings in Ref. [50]. This decrease can be attributed to

the significant reduction in the interaction strength as the separation between the materials increases.

Furthermore, we investigate the impact of increasing background permittivity ϵ_1 in the upper half space on the Rabi splitting. We find that as the background permittivity increases, the Rabi splitting decreases. This can be interpreted as the enhanced screening effect resulting from the increased background permittivity, which weakens the overall interaction.

Lastly, we consider the influence of particle radius on the Rabi splitting, which exhibits a scaling behavior similar to the dependence of the plexcitonic eigenvalues E^{λ} on the radius. Increasing the radius leads to a cubic increase in volume, enhancing the interaction strength. However, this is counteracted by the increase in effective separation, leading to an exponential decrease in the interaction strength.

[1] K. F. Mak, C. Lee, J. Hone, J. Shan, and T. F. Heinz, Atomically thin MoS_2: A new direct-gap semiconductor, Phys. Rev. Lett. **105**, 136805 (2010).

[2] A. Splendiani, L. Sun, Y. Zhang, T. Li, J. Kim, C.-Y. Chim, G. Galli, and F. Wang, Emerging photoluminescence in monolayer MoS_2, Nano Lett. **10**, 1271 (2010).

[3] T. Cao, G. Wang, W. Han, H. Ye, C. Zhu, J. Shi, Q. Niu, P. Tan, E. Wang, and B. Liu, Valley-selective circular dichroism of monolayer molybdenum disulphide, Nat. Commun. **3**, 1 (2012).

[4] D. Xiao, G.-B. Liu, W. Feng, X. Xu, and W. Yao, Coupled spin and valley physics in monolayers of MoS_2 and other group-VI dichalcogenides, Phys. Rev. Lett. **108**, 196802 (2012).

[5] K. Kośmider, J. W. González, and J. Fernández-Rossier, Large spin splitting in the conduction band of transition metal dichalcogenide monolayers, Phys. Rev. B **88**, 245436 (2013).

[6] N. S. Rytova, Screened potential of a point charge in a thin film, Mosc. Univ. Phys. Bull. **3** (2018).

[7] L. V. Keldysh, Coulomb interaction in thin semiconductor and semimetal films, JETP Lett. **29**, 658 (1979).

[8] M. Feierabend, G. Berghäuser, A. Knorr, and E. Malic, Proposal for dark exciton based chemical sensors, Nat. Commun. **8**, 14776 (2017).

[9] K. Greben, S. Arora, M. G. Harats, and K. I. Bolotin, Intrinsic and extrinsic defect-related excitons in TMDCs, Nano Lett. **20**, 2544 (2020).

[10] M. Rösner, C. Steinke, M. Lorke, C. Gies, F. Jahnke, and T. O. Wehling, Two-dimensional heterojunctions from nonlocal manipulations of the interactions, Nano Lett. **16**, 2322 (2016).

[11] O. Benson, Assembly of hybrid photonic architectures from nanophotonic constituents, Nature (London) **480**, 193 (2011).

[12] M. Katzer, S. Kovalchuk, K. Greben, K. I. Bolotin, M. Selig, and A. Knorr, Impact of dark excitons on Förster-type resonant energy transfer between dye molecules and atomically thin semiconductors, Phys. Rev. B **107**, 035304 (2023).

[13] D. Christiansen, M. Selig, M. Rossi, and A. Knorr, Optical classification of excitonic phases in molecular functionalized atomically-thin semiconductors, Phys. Rev. B **107**, L041401 (2023).

[14] J. J. P. Thompson, M. Gerhard, G. Witte, and E. Malic, Optical signatures of Förster-induced energy transfer in organic/TMD heterostructures, npj 2D Mater Appl **7**, 69 (2023).

[15] T. Pincelli, T. Vasileiadis, S. Dong, S. Beaulieu, M. Dendzik, D. Zahn, S.-E. Lee, H. Seiler, Y. Qi, R. P. Xian, J. Maklar, E. Coy, N. S. Mueller, Y. Okamura, S. Reich, M. Wolf, L. Rettig, and R. Ernstorfer, Observation of multi-directional energy transfer in a hybrid plasmonic-excitonic nanostructure, Adv. Mater. **35**, 2209100 (2023).

[16] N. S. Mueller and S. Reich, Microscopic theory of optical absorption in graphene enhanced by lattices of plasmonic nanoparticles, Phys. Rev. B **97**, 235417 (2018).

[17] P. Kusch, N. S. Mueller, M. T. Hartmann, and S. Reich, Strong light-matter coupling in MoS_2, Phys. Rev. B **103**, 235409 (2021).

[18] Z.-S. Deng, L.-Y. Li, C.-L. You, Y.-W. Lu, and J.-F. Liu, Effective modes for a strongly coupled quantum emitter-MoS_2 nanodisk system, IEEE Photonics J. **15**, 1 (2023).

[19] A. K. Geim and I. V. Grigorieva, Van der Waals heterostructures, Nature (London) **499**, 419 (2013).

[20] P. Rivera, J. R. Schaibley, A. M. Jones, J. S. Ross, S. Wu, G. Aivazian, P. Klement, K. Seyler, G. Clark, N. J. Ghimire, J. Yan, D. G. Mandrus, W. Yao, and X. Xu, Observation of long-lived interlayer excitons in monolayer $MoSe_2$-WSe_2 heterostructures, Nat. Commun. **6**, 6242 (2015).

[21] S. Ovesen, S. Brem, C. Linderälv, M. Kuisma, T. Korn, P. Erhart, M. Selig, and E. Malic, Interlayer exciton dynamics in van der Waals heterostructures, Commun. Phys. **2**, 23 (2019).

[22] K. Barthelmi, J. Klein, A. Hötger, L. Sigl, F. Sigger, E. Mitterreiter, S. Rey, S. Gyger, M. Lorke, M. Florian, F. Jahnke, T. Taniguchi, K. Watanabe, V. Zwiller, K. D. Jöns, U. Wurstbauer, C. Kastl, A. Weber-Bargioni, J. J. Finley, K. Müller, and A. W. Holleitner, Atomistic defects as single-photon emitters in atomically thin MoS_2, Appl. Phys. Lett. **117**, 070501 (2020)..

[23] P. Tonndorf, R. Schmidt, R. Schneider, J. Kern, M. Buscema, G. A. Steele, A. Castellanos-Gomez, H. S. J. van der Zant, S. Michaelis de Vasconcellos, and R. Bratschitsch, Single-photon emission from localized excitons in an atomically thin semiconductor, Optica **2**, 347 (2015).

[24] Y.-M. He, G. Clark, J. R. Schaibley, Y. He, M.-C. Chen, Y.-J. Wei, X. Ding, Q. Zhang, W. Yao, X. Xu, C.-Y. Lu, and J.-W. Pan, Single quantum emitters in monolayer semiconductors, Nat. Nanotechnol. **10**, 497 (2015).

[25] K. L. Seyler, P. Rivera, H. Yu, N. P. Wilson, E. L. Ray, D. G. Mandrus, J. Yan, W. Yao, and X. Xu, Signatures of moiré-trapped valley excitons in $MoSe_2/WSe_2$ heterobilayers, Nature (London) **567**, 66 (2019).

[26] F. Mahdikhanysarvejahany, D. N. Shanks, M. Klein, Q. Wang, M. R. Koehler, D. G. Mandrus, T. Taniguchi, K. Watanabe, O. L. A. Monti, B. J. LeRoy, and J. R. Schaibley, Localized interlayer excitons in $MoSe_2$-WSe_2 heterostructures without a moiré potential, Nat. Commun. **13**, 5354 (2022).

[27] T. Gao, M. von Helversen, C. Antón-Solanas, C. Schneider, and T. Heindel, Atomically-thin single-photon sources for quantum communication, npj 2D Mater. Appl. **7**, 4 (2023).

[28] J.-Y. Li, W. Li, J. Liu, J. Zhong, R. Liu, H. Chen, and X.-H. Wang, Room-temperature strong coupling between a single quantum dot and a single plasmonic nanoparticle, Nano Lett. **22**, 4686 (2022).

[29] A. I. Fernández-Domínguez, S. I. Bozhevolnyi, and N. A. Mortensen, Plasmon-enhanced generation of nonclassical light, ACS Photonics **5**, 3447 (2018).

[30] S. Franke, M. Richter, J. Ren, A. Knorr, and S. Hughes, Quantized quasinormal-mode description of nonlinear cavity-QED effects from coupled resonators with a Fano-like resonance, Phys. Rev. Res. **2**, 033456 (2020).

[31] A. Manjavacas, F. J. García de Abajo, and P. Nordlander, Quantum plexcitonics: Strongly interacting plasmons and excitons, Nano Lett. **11**, 2318 (2011).

[32] Y. Sang, C.-Y. Wang, S. S. Raja, C.-W. Cheng, C.-T. Huang, C.-A. Chen, X.-Q. Zhang, H. Ahn, C.-K. Shih, Y.-H. Lee, J. Shi, and S. Gwo, Tuning of two-dimensional plasmon-exciton coupling in full parameter space: A polaritonic non-Hermitian system, Nano Lett. **21**, 2596 (2021).

[33] X. Xiong, N. Kongsuwan, Y. Lai, C. E. Png, L. Wu, and O. Hess, Room-temperature plexcitonic strong coupling: Ultrafast dynamics for quantum applications, Appl. Phys. Lett. **118**, 130501 (2021).

[34] W. Zhang, J.-B. You, J. Liu, X. Xiong, Z. Li, C. E. Png, L. Wu, C.-W. Qiu, and Z.-K. Zhou, Steering room-temperature plexcitonic strong coupling: A diexcitonic perspective, Nano Lett. **21**, 8979 (2021).

[35] H. Deng, G. Weihs, C. Santori, J. Bloch, and Y. Yamamoto, Condensation of semiconductor microcavity exciton polaritons, Science **298**, 199 (2002).

[36] H. Deng, H. Haug, and Y. Yamamoto, Exciton-polariton Bose-Einstein condensation, Rev. Mod. Phys. **82**, 1489 (2010).

[37] M.-E. Kleemann, R. Chikkaraddy, E. M. Alexeev, D. Kos, C. Carnegie, W. Deacon, A. C. de Pury, C. Große, B. de Nijs, J. Mertens, A. I. Tartakovskii, and J. J. Baumberg, Strong-coupling of WSe_2 in ultra-compact plasmonic nanocavities at room temperature, Nat. Commun. **8**, 1296 (2017).

[38] H. Groß, J. M. Hamm, T. Tufarelli, O. Hess, and B. Hecht, Near-field strong coupling of single quantum dots, Sci. Adv. **4**, eaar4906 (2018).

[39] J. J. Baumberg, J. Aizpurua, M. H. Mikkelsen, and D. R. Smith, Extreme nanophotonics from ultrathin metallic gaps, Nat. Mater. **18**, 668 (2019).

[40] Y. Zhu, J. Yang, J. Abad-Arredondo, A. I. Fernández-Domínguez, F. J. Garcia-Vidal, and D. Natelson, Electroluminescence as a probe of strong exciton-plasmon coupling in few-layer WSe_2, arXiv:2302.00023.

[41] X. Han, K. Wang, X. Xing, M. Wang, and P. Lu, Rabi splitting in a plasmonic nanocavity coupled to a WS_2 monolayer at room temperature, ACS Photonics **5**, 3970 (2018).

[42] M. Geisler, X. Cui, J. Wang, T. Rindzevicius, L. Gammelgaard, B. S. Jessen, P. A. D. Gonçalves, F. Todisco, P. Bøggild, A. Boisen, M. Wubs, N. A. Mortensen, S. Xiao, and N. Stenger, Single-crystalline gold nanodisks on WS_2 mono- and multilayers for strong coupling at room temperature, ACS Photonics **6**, 994 (2019).

[43] M. Stührenberg, B. Munkhbat, D. G. Baranov, J. Cuadra, A. B. Yankovich, T. J. Antosiewicz, E. Olsson, and T. Shegai, Strong light-matter coupling between plasmons in individual gold bi-pyramids and excitons in mono- and multilayer WSe_2, Nano Lett. **18**, 5938 (2018).

[44] J. Wen, H. Wang, W. Wang, Z. Deng, C. Zhuang, Y. Zhang, F. Liu, J. She, J. Chen, H. Chen, S. Deng, and N. Xu, Room-temperature strong light-matter interaction with active control in single plasmonic nanorod coupled with two-dimensional atomic crystals, Nano Lett. **17**, 4689 (2017).

[45] J. Qin, Y.-H. Chen, Z. Zhang, Y. Zhang, R. J. Blaikie, B. Ding, and M. Qiu, Revealing strong plasmon-exciton coupling between nanogap resonators and two-dimensional semiconductors at ambient conditions, Phys. Rev. Lett. **124**, 063902 (2020).

[46] I. Abid, W. Chen, J. Yuan, A. Bohloul, S. Najmaei, C. Avendano, R. Péchou, A. Mlayah, and J. Lou, Temperature-dependent plasmon-exciton interactions in hybrid Au/$MoSe_2$ nanostructures, ACS Photonics **4**, 1653 (2017).

[47] X. Wu, S. K. Gray, and M. Pelton, Quantum-dot-induced transparency in a nanoscale plasmonic resonator, Opt. Express **18**, 23633 (2010).

[48] P. Törmä and W. L. Barnes, Strong coupling between surface plasmon polaritons and emitters: A review, Rep. Prog. Phys. **78**, 013901 (2015).

[49] E. V. Denning, M. Wubs, N. Stenger, J. Mørk, and P. T. Kristensen, Quantum theory of two-dimensional materials coupled to electromagnetic resonators, Phys. Rev. B **105**, 085306 (2022).

[50] C. Carlson, R. Salzwedel, M. Selig, A. Knorr, and S. Hughes, Strong coupling regime and hybrid quasinormal modes from a single plasmonic resonator coupled to a transition metal dichalcogenide monolayer, Phys. Rev. B **104**, 125424 (2021).

[51] P. G. Etchegoin, E. C. Le Ru, and M. Meyer, An analytic model for the optical properties of gold, J. Chem. Phys. **125**, 164705 (2006).

[52] G. Mie, Beiträge zur Optik trüber Medien, speziell kolloidaler Metallösungen, Ann. Phys. (Berlin, Ger.) **330**, 377 (1908).

[53] R. Gans, Über die form ultramikroskopischer goldteilchen, Ann. Phys. (Berlin, Ger.) **342**, 881 (1912).

[54] M. Selig, F. Katsch, R. Schmidt, S. Michaelis de Vasconcellos, R. Bratschitsch, E. Malic, and A. Knorr, Ultrafast dynamics in monolayer transition metal dichalcogenides: Interplay of dark excitons, phonons, and intervalley exchange, Phys. Rev. Res. **1**, 022007(R) (2019).

[55] F. Katsch, M. Selig, A. Carmele, and A. Knorr, Theory of exciton-exciton interactions in monolayer transition metal dichalcogenides, Phys. Status Solidi B **255**, 1800185 (2018).

[56] A. Knorr, S. Hughes, T. Stroucken, and S. Koch, Theory of ultrafast spatio-temporal dynamics in semiconductor heterostructures, Chem. Phys. **210**, 27 (1996).

[57] M. Selig, G. Berghäuser, A. Raja, P. Nagler, C. Schüller, T. F. Heinz, T. Korn, A. Chernikov, E. Malic, and A. Knorr, Excitonic linewidth and coherence lifetime in monolayer transition metal dichalcogenides, Nat. Commun. **7**, 13279 (2016).

[58] G. Cappellini, R. Del Sole, L. Reining, and F. Bechstedt, Model dielectric function for semiconductors, Phys. Rev. B **47**, 9892 (1993).

[59] M. L. Trolle, T. G. Pedersen, and V. Véniard, Model dielectric function for 2D semiconductors including substrate screening, Sci. Rep. **7**, 39844 (2017).

[60] M. Kira and S. Koch, Many-body correlations and excitonic effects in semiconductor spectroscopy, Prog. Quantum Electron. **30**, 155 (2006).

[61] D. Y. Qiu, T. Cao, and S. G. Louie, Nonanalyticity, valley quantum phases, and lightlike exciton dispersion in monolayer transition metal dichalcogenides: Theory and first-principles calculations, Phys. Rev. Lett. **115**, 176801 (2015).

[62] P. B. Johnson and R. W. Christy, Optical constants of the noble metals, Phys. Rev. B **6**, 4370 (1972).

[63] C. Cirací, R. T. Hill, J. J. Mock, Y. Urzhumov, A. I. Fernández-Domínguez, S. A. Maier, J. B. Pendry, A. Chilkoti, and D. R. Smith, Probing the ultimate limits of plasmonic enhancement, Science **337**, 1072 (2012).

[64] S. Raza, S. I. Bozhevolnyi, M. Wubs, and N. A. Mortensen, Nonlocal optical response in metallic nanostructures, J. Phys.: Condens. Matter **27**, 183204 (2015).

[65] C. Van Vlack, P. T. Kristensen, and S. Hughes, Spontaneous emission spectra and quantum light-matter interactions from a strongly coupled quantum dot metal-nanoparticle system, Phys. Rev. B **85**, 075303 (2012).

[66] A. D. Humphrey and W. L. Barnes, Plasmonic surface lattice resonances on arrays of different lattice symmetry, Phys. Rev. B **90**, 075404 (2014).

[67] A. Moroz, Depolarization field of spheroidal particles, J. Opt. Soc. Am. B **26**, 517 (2009).

[68] A. Delga, J. Feist, J. Bravo-Abad, and F. Garcia-Vidal, Quantum emitters near a metal nanoparticle: Strong coupling and quenching, Phys. Rev. Lett. **112**, 253601 (2014).

[69] L. Zhao, K. L. Kelly, and G. C. Schatz, The extinction spectra of silver nanoparticle arrays: Influence of array structure on plasmon resonance wavelength and width, J. Phys. Chem. B **107**, 7343 (2003).

[70] F. J. García De Abajo, Colloquium: Light scattering by particle and hole arrays, Rev. Mod. Phys. **79**, 1267 (2007).

[71] S. Baur, S. Sanders, and A. Manjavacas, Hybridization of lattice resonances, ACS Nano **12**, 1618 (2018).

[72] R. Carminati, J.-J. Greffet, C. Henkel, and J. Vigoureux, Radiative and non-radiative decay of a single molecule close to a metallic nanoparticle, Opt. Commun. **261**, 368 (2006).

[73] E. B. Barros, B. G. Vieira, N. S. Mueller, and S. Reich, Plasmon-polaritons in nanoparticle supercrystals: Microscopic quantum theory beyond the dipole approximation, Phys. Rev. B **104**, 035403 (2021).

[74] M. M. Glazov, T. Amand, X. Marie, D. Lagarde, L. Bouet, and B. Urbaszek, Exciton fine structure and spin decoherence in monolayers of transition metal dichalcogenides, Phys. Rev. B **89**, 201302(R) (2014).

[75] F. J. García de Abajo, Optical excitations in electron microscopy, Rev. Mod. Phys. **82**, 209 (2010).

[76] H. Haug and S. W. Koch, *Quantum Theory of the Optical and Electronic Properties of Semiconductors*, 4th ed. (World Scientific, Singapore, River Edge, 2004).

[77] M. Lindberg and S. W. Koch, Effective Bloch equations for semiconductors, Phys. Rev. B **38**, 3342 (1988).

[78] N. Moiseyev, *Non-Hermitian Quantum Mechanics* (Cambridge University Press, Cambridge, 2011).

[79] I. Gilary, A. Fleischer, and N. Moiseyev, Calculations of time-dependent observables in non-Hermitian quantum mechanics: The problem and a possible solution, Phys. Rev. A **72**, 012117 (2005).

[80] G. Berghäuser and E. Malic, Analytical approach to excitonic properties of MoS_2, Phys. Rev. B **89**, 125309 (2014).

[81] H. Barkay and N. Moiseyev, Complex density probability in non-Hermitian quantum mechanics: Interpretation and a formula for resonant tunneling probability amplitude, Phys. Rev. A **64**, 044702 (2001).

[82] J. P. Reithmaier, G. Se, S. Reitzenstein, L. V. Keldysh, V. D. Kulakovskii, T. L. Reinecke, and A. Forchel, Strong coupling in a single quantum dot-semiconductor microcavity system, Nature (London) **432**, 197 (2004).

[83] T. Yoshie, A. Scherer, J. Hendrickson, G. Khitrova, H. M. Gibbs, G. Rupper, C. Ell, O. B. Shchekin, and D. G. Deppe, Vacuum Rabi splitting with a single quantum dot in a photonic crystal nanocavity, Nature (London) **432**, 200 (2004).

[84] G. Khitrova, H. M. Gibbs, M. Kira, S. W. Koch, and A. Scherer, Vacuum Rabi splitting in semiconductors, Nat. Phys. **2**, 81 (2006).

[85] A. Kormányos, G. Burkard, M. Gmitra, J. Fabian, V. Zólyomi, N. D. Drummond, and V. Fal'ko, $\mathbf{k} \cdot \mathbf{p}$ theory for two-dimensional transition metal dichalcogenide semiconductors, 2D Mater. **2**, 022001 (2015).

[86] J. D. Jackson, *Classical Electrodynamics*, 5th ed. (De Gruyter, Boston, 1999).

[87] A. Knorr, B. Hanewinkel, H. Giessen, and S. W. Koch, Theory for semiconductor near-field optics: Selection rules and coherent spatio-temporal dynamics, in *Advances in Solid State Physics 38*, edited by B. Kramer (Springer, Berlin, Heidelberg, 1999), Vol. 38, pp. 311–323.